THEORETICAL AND EXPERIMENTAL STUDY OF A FINITE CYLINDRICAL ANTENNA IN A PLASMA COLUMN

By

Chung-Yu Ting, B. Rama Rao, and W.A. Saxton

N67-35956

(ACCESSION NUMBER) (THRU)

53 1

(PAGES) (CODE)

CR-88202 25

(NASA CR OR TMX OR AD NUMBER) (CATEGORY)

FACILITY FORM 602

GPO PRICE $ _____

CFSTI PRICE(S) $ _____

Hard copy (HC) 3.00

Microfiche (MF) .65

ff 653 July 65

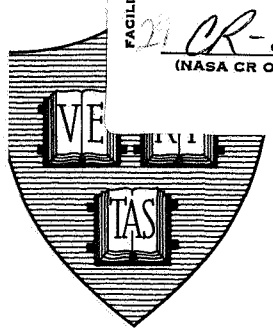

Scientific Report No. 1

July 1967

"Reproduction in whole or in part is permitted by the U. S. Government. Distribution of this document is unlimited."

NATIONAL AERONAUTICS AND SPACE ADMINISTRATION

Prepared under Grant NGR 22-007-056

Division of Engineering and Applied Physics

Harvard University • Cambridge, Massachusetts

THEORETICAL AND EXPERIMENTAL STUDY OF A FINITE CYLINDRICAL ANTENNA IN A PLASMA COLUMN

by

Chung-Yu Ting, B. Rama Rao, and W. A. Saxton

Scientific Report No. 1

Reproduction in whole or in part is permitted by the U.S. Government. Distribution of this document is unlimited.

July 1967

Prepared under Grant NGR-22-007-056
Division of Engineering and Applied Physics
Harvard University, Cambridge, Massachusetts

for

NATIONAL AERONAUTICS AND SPACE ADMINISTRATION

THEORETICAL AND EXPERIMENTAL STUDY OF A FINITE CYLINDRICAL ANTENNA IN A PLASMA COLUMN

Chung-Yu Ting, B. Rama Rao, and W. A. Saxton
Harvard University

ABSTRACT

A finite cylindrical antenna in an infinite plasma column is investigated both theoretically and experimentally. In the theoretical analysis, the plasma is approximated as a dielectric medium with relative dielectric constant $1 - \omega_p^2/\omega^2$. The current distributions as well as the input admittances are obtained by a numerical method for both the cases $\omega > \omega_p$ and $\omega < \omega_p$.

Experimental work is done by extending a coaxially driven cylindrical antenna into a coaxial glass tube which contains the plasma. Langmuir probe and cavity perturbation techniques are used in the diagnostic measurements. The current distributions and input admittances of the antenna have been measured for various pressures and discharge currents. The experimental results show a reasonable degree of qualitative agreement with the theoretical results.

THEORETICAL AND EXPERIMENTAL STUDY OF A FINITE CYLINDRICAL ANTENNA IN A PLASMA COLUMN

Chung-Yu Ting, B. Rama Rao, and W. A. Saxton
Harvard University

I. INTRODUCTION

The purpose of this paper is to study both theoretically and experimentally the near-field characteristics of an antenna when it is covered by a layer of ionized gas or "plasma sheath." As in the case of a re-entry vehicle, it is a well known fact that this plasma sheath has greatly affected the radiocommunication as well as the antenna itself.

A similar problem in which a point dipole in an infinite plasma column is investigated was discussed theoretically by Seshadri [1]. In this study, a numerical method is used to solve the problem of a finite cylindrical antenna in an infinite plasma column. To make the problem mathematically tractable, a highly idealized plasma model is assumed in the analysis; collision losses and electron temperature effects are ignored; and the plasma column is also assumed to be radially homogeneous. Under these simplfying assumptions, the "cold" plasma behaves like a dielectric medium with a relative dielectric constant $\epsilon_r = 1 - \omega_p^2 / \omega^2$. It is found that when $0 < \epsilon_r < 1$ the plasma behaves essentially like a lossless medium and tends to reduce the effective electrical length of the antenna. The current distribution is still approximately sinusoidal but with a longer wavelength. In the range $-1 < \epsilon_r < 0$, the antenna characteristics undergo a drastic change. The current attenuates very rapidly along the length of the antenna. When the antenna is longer than a quarter-wavelength, it behaves much like an infinite one with an input admittance remaining almost constant and independent of the antenna length.

Extensive experimental measurements have been made to verify the theory. The plasma sheath surrounding the antenna was produced by means of a hot-cathode, d.c. discharge contained within a long coaxial glass tube. The inner

glass tube served as a d.c. insulating sleeve around the antenna, so that no d.c. current was drawn from the discharge by the antenna. The current distribution and input admittance of the antenna were measured by a small shielded loop probe which traveled along a narrow slot in the antenna. The electron density, electron temperature, and collision frequency were measured using Langmuir probes and the microwave-cavity perturbation technique. The experimental results show a reasonable degree of qualitative agreement with the theoretical results. It is also noticed that the input resistance of a very short dipole shows a strong "resonance" phenomenon at a frequency below the plasma frequency.

II. A THEORETICAL STUDY OF A PLASMA-COATED FINITE ANTENNA

Consider the cylindrical dipole in a plasma column as shown in Fig. 1. The antenna has a radius 'a' and length 2h, while the plasma column is infinitely long and has a radius 'b'. The plasma is highly idealized: the losses due to collisions, the anisotropy due to the earth's magnetic field, the pressure gradient due to the finite temperature, and the inhomogeneity caused by the radial variation in electron density are all neglected. Under these assumptions the plasma essentially behaves like a dielectric medium with a relative dielectric constant $\epsilon_r = 1 - \omega^2/\omega_p^2$, which is always smaller than one and can become negative when the operating frequency ω is smaller than the plasma frequency ω_p. The numerical method used to solve the integral equation of a finite cylindrical antenna in an infinitely long dielectric rod [2] is used. The mathematical analysis is the same, but the singularities of the Fourier-transformed Green's function are somewhat different. This will be discussed separately.

A. For the Case $\omega > \omega_p$

The procedures discussed in [2] in which the Fourier transform pair is defined by

$$\overline{F}(k) = \int_{-\infty}^{\infty} f(z)\, e^{ikz}\, dz \qquad (1a)$$

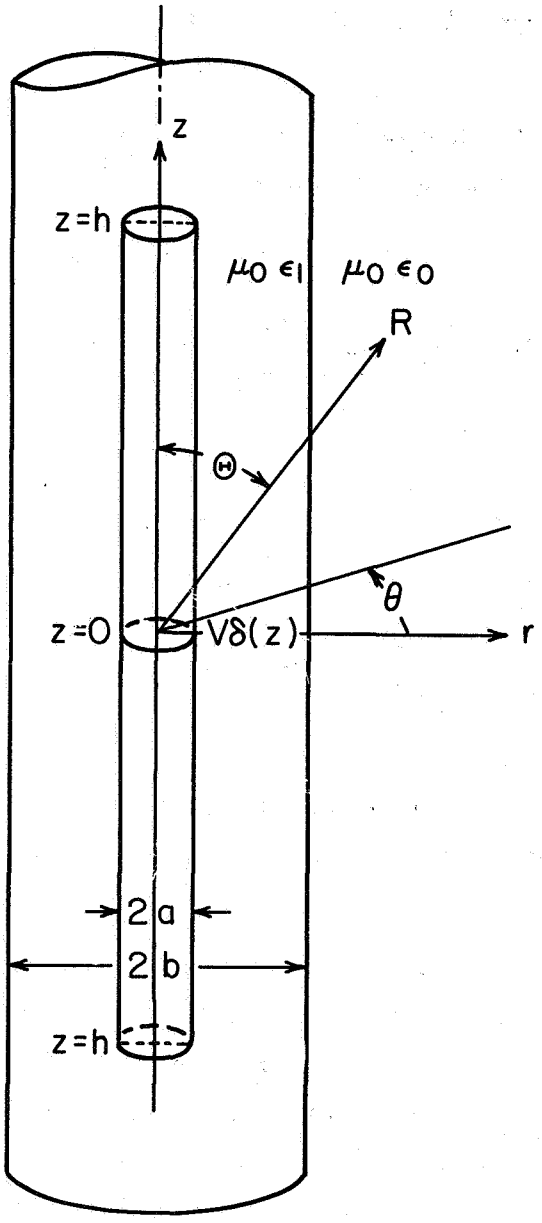

FIG. 1 A SCHEMATIC DIAGRAM OF A FINITE DIPOLE IN AN INFINITE PLASMA COLUMN

$$f(z) = \frac{1}{2\pi} \int_{-\infty}^{\infty} \overline{F}(k)\, e^{-ikz}\, dk \qquad (1b)$$

lead to the following Fourier transformed Green's function of the vector potential at $r = a$ due to a ring current source $\frac{\hat{z}}{2\pi a}\,\delta(r-a)\,\delta(z)$:

$$\overline{G}(k, a) = -\frac{\mu_0 J_0(\xi a)\quad -\xi H_1^{(1)}(\psi b)\,[J_0(\xi a) Y_0(\xi b) - J_0(\xi b) Y_0(\xi a)]\}}{4\,[\xi J_0(\xi b) H_1^{(1)}(\psi b) - \epsilon_r \psi J_1(\xi b) H_0^{(1)}(\psi b)]} \qquad (2)$$

where

$$\psi = \sqrt{k_0^2 - k^2}\ , \quad \xi = \sqrt{k_1^2 - k^2}\ , \quad k_0 = \omega\sqrt{\mu_0\epsilon_0}\ , \quad k_1 = \omega\sqrt{\mu_0\epsilon_1}$$

$$\epsilon_1 = \epsilon_0\epsilon_r = \epsilon_0\left(1 - {\omega_p^2}/{\omega^2}\right).$$

The permeability of the free space is μ_0 , and ϵ_0 , ϵ_1 are the dielectric constants of the free space and the plasma medium. J and Y are the Bessel functions of the first and second kind; H is the Hankel function; and the time dependence is $e^{-i\omega t}$.

$\overline{G}(k, a)$ has two branch points at $k = \pm k_0$. Points $k = \pm k_1$ are not branch points, but are two simple poles. Other poles and zeros can be determined by the zeros of the denominator and numerator, which have been discussed in detail by Tamir and Palócz [3]. When equaled to zero, the denominator gives the dispersion equation of a plasma column which can support a surface wave mode only at $\omega < \omega_p/\sqrt{2}$ $(\epsilon_r < -1)$. The numerator, when equaled to zero, gives the dispersion equation of a plasma-clad metal rod, which may have one, two, or three zeros in the region $\omega < \omega_p$ $(\epsilon_r < 0)$, depending on the geometry. Therefore, in the region $\omega > \omega_p$ $(1 > \epsilon_r > 0)$, a method similar to that discussed in [4] can be used to prove that $\overline{G}(k, a)$ has no singularity on the whole k-plane, except two branch points at $k = \pm k_0$ and two simple poles at $k = \pm k_1$ as

shown in Fig. 2. The result is

$$G(z, a) = P\Bigg[\int_0^{k_1} \frac{i\mu_0 \varepsilon_r [J_0^2(Qa)]^2 e^{ixz}\, dx}{\pi^3 b^2 \{[Q J_0(Qb) J_1(Pb) - \varepsilon_r P J_1(Qb) J_0(Pb)]^2 + [Q J_0(Qb) Y_1(Pb) - \varepsilon_r J_1(Qb) Y_0(Pb)]^2\}}$$

$$+ \int_{k_1}^{k_0} \frac{-i\mu_0 \varepsilon_r [I_0(a a)]^2 e^{ixz}\, dx}{\pi^3 b^2 \{[a I_0(a b) J_1(P b) - \varepsilon_r P I_1(a b) J_0(Pb)]^2 + [a I_0(a b) Y_1(Pb) - \varepsilon_r P I_1(a b) Y_0(Pb)]^2\}} \Bigg]$$

$$+ \int_0^{\infty} \frac{4\varepsilon_r [J_0(Va)]^2 e^{-yz}\, dy}{\pi^3 b^2 \{[V J_0(Vb) J_1(Ub) - \varepsilon_r U J_1(Vb) J_0(Ub)]^2 + [V J_0(Vb) Y_1(Ub) - \varepsilon_r U J_1(Vb) Y_0(Ub)]^2\}}$$

$$\{2[J_0(\gamma b) J_1(\gamma b) + Y_0(\gamma b) Y_1(\gamma b)]$$

$$- \frac{i k_1 \gamma b \quad -\varepsilon_r \gamma b [J_0(\gamma b)]^2 + \varepsilon_r \gamma b [Y_0(\gamma b)]^2\} e^{i k_1 z}}{k_0^2 b^2 \{[2J_1(\gamma b) - \varepsilon_r \gamma b J_0(\gamma b)]^2 + [2Y_1(\gamma b) - \varepsilon_r \gamma b Y_0(\gamma b)]^2\}} \qquad (3)$$

where I_0, I_1 are the modified Bessel functions of zero and first order, and

$$a = \sqrt{x^2 - k_1^2}\,, \qquad P = \sqrt{k_0^2 - x^2}\,, \qquad Q = \sqrt{k_1^2 - x^2}$$

$$U = \sqrt{k_0^2 + y^2}\,, \qquad V = \sqrt{k_1^2 + y^2}\,. \qquad \gamma = \sqrt{k_0^2 - k_1^2}$$

Hallen's integral equation of the antenna shown in Fig. 1, in this case is

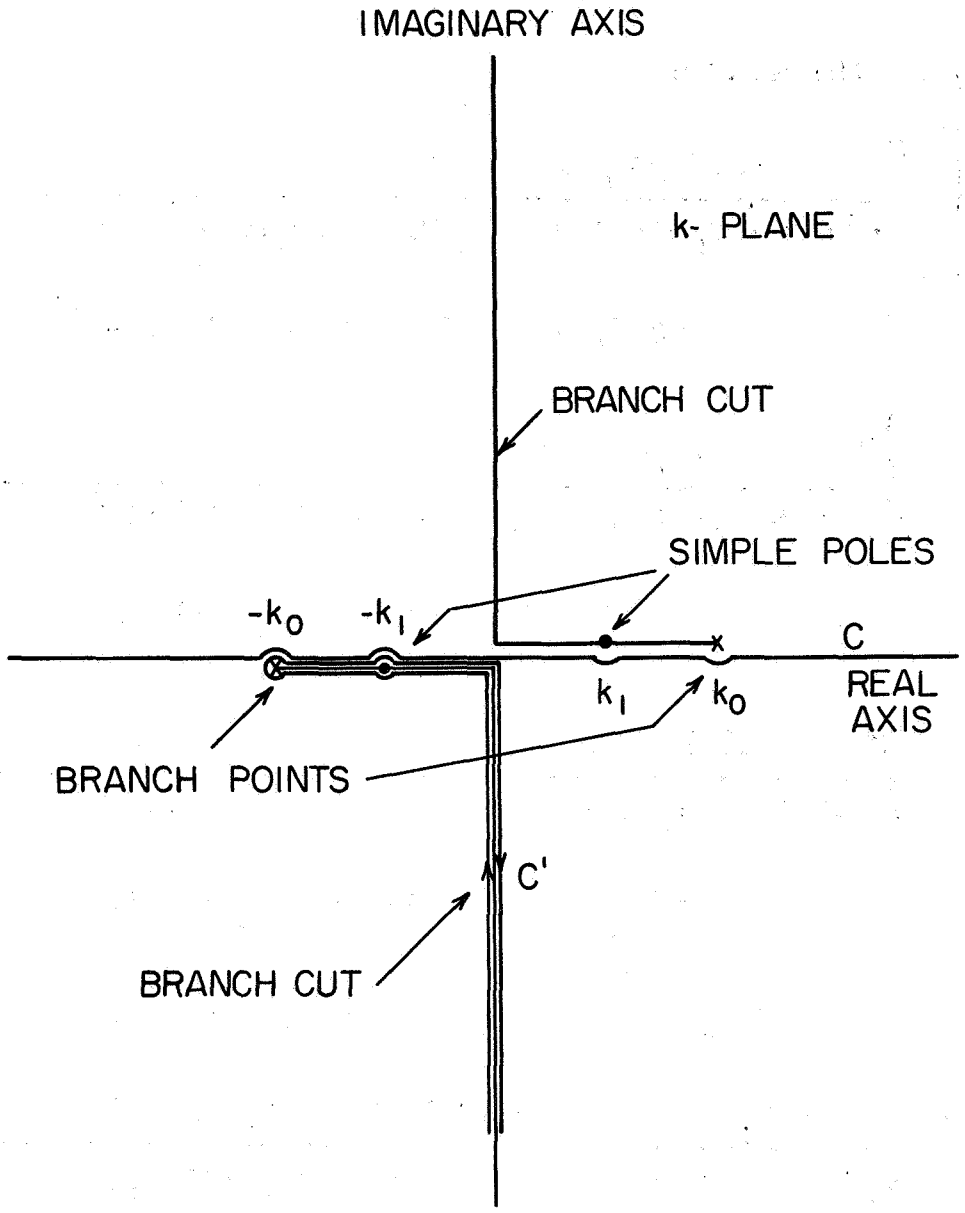

FIG. 2 SINGULARITIES OF $\bar{G}(k, a)$ FOR $1 > \epsilon_r > 0$ AND INTEGRATION PATHS C, C'

$$\int_{-h}^{h} \frac{4\pi}{\mu_0} I(z') G(z - z', a)\, dz' = \frac{i4\pi}{\zeta_1} \left[C \cos k_1 z + \frac{V}{2} \sin k_1 |z| \right] \qquad (4)$$

where $\zeta_1 = \sqrt{\mu_0/\epsilon_1}$, C is a constant to be determined by the condition that the axial current vanishes at $z = \pm h$.

B. For the Case $\omega_p > \omega > \frac{\omega_p}{\sqrt{2}}$

The Green's function in this case is identical to (2), except that $\epsilon_r = 1 - \omega_p^2/\omega^2$ is now negative and greater than -1 . Nevertheless, the singularities on the k-plane are different. There are poles in the finite complex k-plane and at infinity. Since the condition of a pole at large $|k|$, as given in [2], is

$$\sqrt{k^2 - k_1^2}\, b + i \frac{\pi}{4} = \frac{1}{2} \ell n \frac{1 - \epsilon_r}{1 + \epsilon_r} + in\pi \qquad (5)$$

where $\sqrt{k^2 - k_1^2}$ takes the positive sign when k is positive and large, and n is a large integer. Equation (5) can be satisfied, and it has an infinite number of solutions as n goes to infinity. Consequently, the Fourier inverse integral cannot be closed at infinity unless the locations of all of these poles and their residues are known. An alternate expression of (2), which can help the numerical calculation is given by

$$\overline{G}_2(k, a) = i \frac{\mu_0}{4} \left\{ \frac{J_0^2(\xi a)[\epsilon_r \psi H_1^{(1)}(\xi b) H_0^{(1)}(\psi b) - \xi H_0^{(1)}(\xi b) H_1^{(1)}(\psi b)]}{\xi J_0(\xi b) H_1^{(1)}(\psi b) - \epsilon_r \psi J_1(\xi b) H_0^{(1)}(\psi b)} \right\} + i \frac{\mu_0}{4} J_0(\xi a) H_0^{(1)}(\xi a) \qquad (6)$$

The first term, which involves an infinite number of poles on the k-plane, decays exponentially on the real axis as $k \to \pm \infty$. The second term, which has no pole anywhere, has two branch points at $k = \pm k_1$ on the imaginary axis. In carrying out the Fourier inverse integral, the contour of integration of the first

term is kept on the real axis, and that of the second term is deformed around the branch cut as shown in Fig. 3. Since $0 > \varepsilon_r > -1$, there is no pole on the real axis, as mentioned before. After the real and imaginary parts have been separated, the Green's function becomes

$$G_2(z, a) =$$

$$\frac{\mu_0}{2\pi^2}\int_{k_0}^{\infty} \frac{I_0^2(\alpha a)[\varepsilon_r \beta K_1(\alpha b) K_0(\beta b) - \alpha K_0(\alpha b) K_1(\beta b)}{\alpha I_0(\alpha b) K_1(\alpha b) + \varepsilon_r \beta I_1(\alpha b) K_0(\beta b)} \cos(xz)\, dx$$

$$I_0^2(\alpha a)\{[\alpha K_0(\alpha b) J_1(Pb) +$$

$$+ \varepsilon_r P K_1(\alpha b) J_0(Pb)][\alpha I_0(\alpha b) J_1(Pb) - \varepsilon_r P I_1(\alpha b) J_0(Pb)] +$$

$$+ [\alpha K_0(\alpha b) Y_1(Pb) + \varepsilon_r P K_1(\alpha b) Y_0(Pb)][\alpha I_0(\alpha b) Y_1(Pb) -$$

$$- \frac{\mu_0}{2\pi^2}\int_0^{k_0} \frac{\varepsilon_r P I_1(\alpha b) Y_0(Pb)]\}}{[\alpha I_0(\alpha b) J_1(Pb) - \varepsilon_r P I_1(\alpha b) J_0(Pb)]^2 +} \cos(xz)\, dx$$

$$+[\alpha I_0(\alpha b) Y_1(Pb) - \varepsilon_r P I_1(\alpha b) Y_0(Pb)]^2$$

$$+ \frac{\mu_0}{4\pi}\int_{|k_1|}^{\infty} J_0^2(Ua) e^{-yz}\, dy$$

$$- i\frac{\mu_0 \varepsilon_r}{\pi^3 b^2}\int_0^{k_0} \frac{I_0^2(\alpha a) \cos(xz)\, dx}{[\alpha I_0(\alpha b) J_1(Pb) - \varepsilon_r P I_1(\alpha b) I_0(Pb)]^2 +}$$

$$+[\alpha I_0(\alpha b) Y_1(Pb) - \varepsilon_r P I_1(\alpha b) Y_1(Pb)]^2$$

(7)

where K_0 and K_1 are the modified Henkel function of zero and first orders, $\beta = \sqrt{x^2 - k_1^2}$, α, P, U are the same as before. Hallen's integral equation,

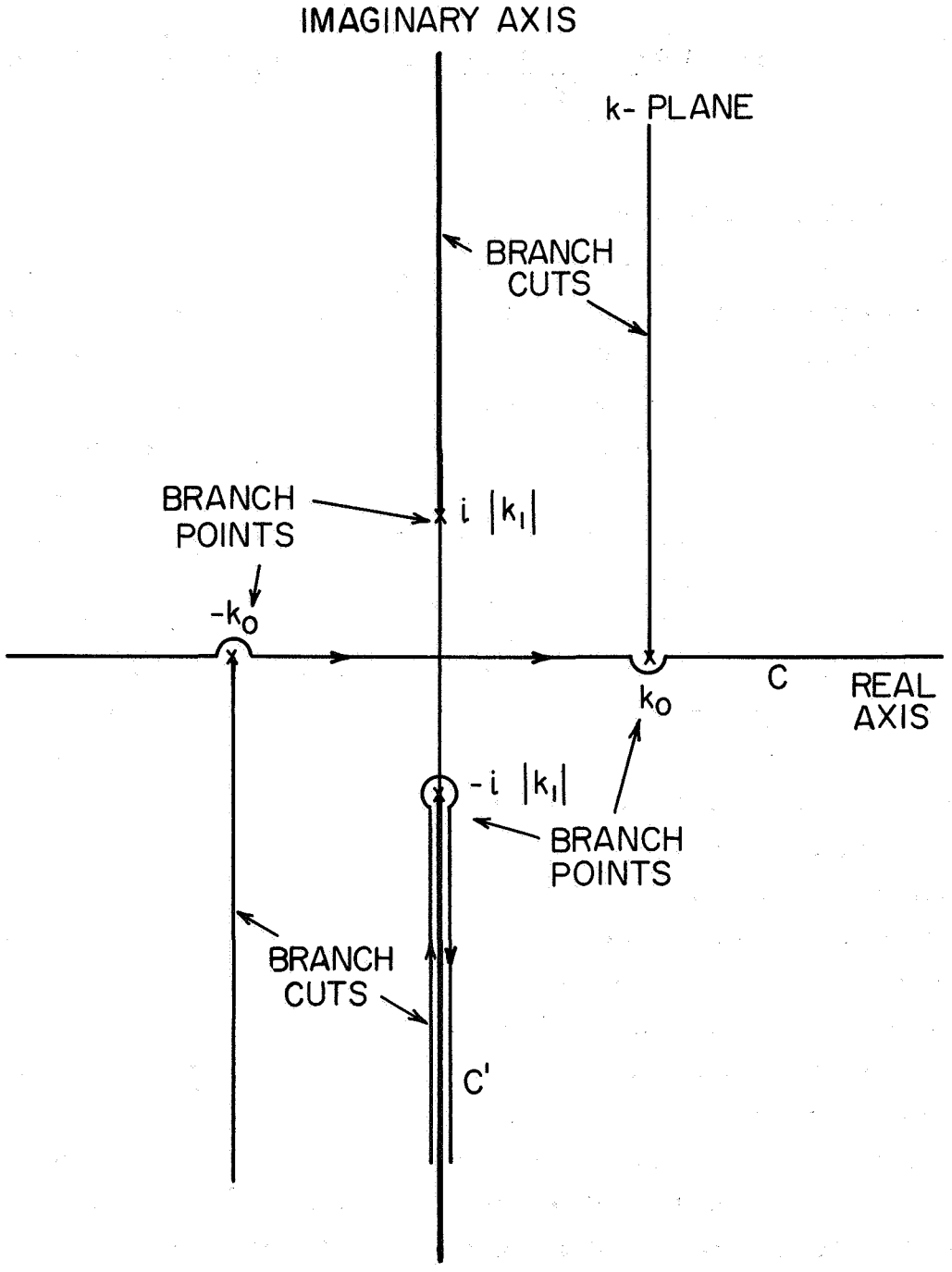

FIG. 3 SINGULARITIES OF $\bar{G}(k, a)$ FOR $0 > \epsilon r > -1$ AND INTEGRATION PATHS C, C'

in this case, becomes

$$\int_{-h}^{h} \frac{4\pi}{\mu_0} I(z')\, G(z - z', a)\, dz' = \frac{i4\pi}{\sqrt{\mu_0/|\epsilon_1|}} \left[C_1 \cosh(|k_1|z) + \frac{V}{2} \sinh(|k_1 z|) \right] \qquad (8)$$

C. Numerical Results

The numerical method used to solve the integral equations (4) and (8) is the same as that used to solve the dielectric-coated antenna. In short, the antenna is divided into a number of subintervals. Within each subinterval, the current is approximated by expanding it into a power series of order 3 about the midpoint of the subinterval. In this way, the integral equation can be converted into a set of linear equations. Solutions are found by a matrix-inversion method. In the first case, a typical example, $\omega = \sqrt{2}\,\omega_p$ ($\epsilon_r = 0.5$), $b/a = 4$, $k_0 a = 0.04$, is given. Twenty-four current distributions for different lengths were calculated, three of which, $k_0 h = 3\pi/2$, $k_0 h = \pi$, and $k_0 h = 3\pi/2$, are shown in Fig. 4. It is noted that in these cases the current distributions are still approximately sinusoidal, but that the effective wavelength is longer and close to the free space wavelength divided by $\sqrt{\epsilon_r}$. The effective length of the antenna is shortened instead of lengthened as in the case of an antenna with a dielectric coating with $\epsilon_r > 1$. In the second case, an example is given by using the parameters $\omega = \sqrt{\frac{2}{3}}\,\omega_p$ ($\epsilon_r = -0.5$), $b/a = 4$, $k_0 a = 0.04$. Since in this case part of the integration is carried out on the real axis, extremely long computing time is needed. Calculations were made for current distributions along antennas with 16 different lengths, of which $k_0 h = \pi/4$, $k_0 h = \pi/2$, $k_0 h = \pi$ are shown in Fig. 5. It is of great interest to note the drastic change in the current distribution, the magnitude of which, like the field in a waveguide below cutoff, now attenuates very rapidly along the length of the antenna; the phase of antenna current, contrary to the conventional case, increases along the length of the antenna. For an antenna with length shorter then $\lambda_0/8$, the triangular current distribution certainly is a very good approximation. If the current at the driving point divided by the driving point voltage is defined as

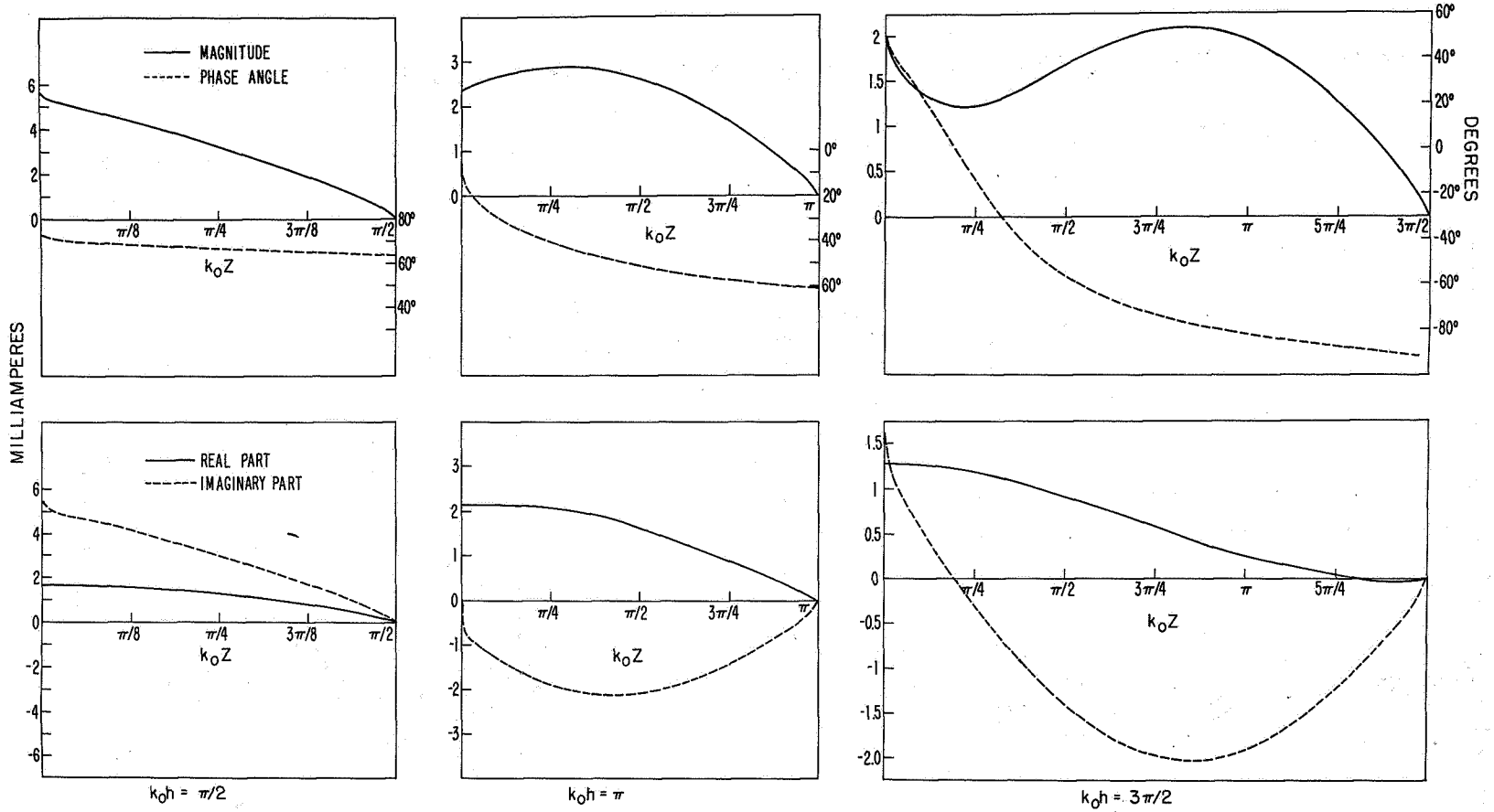

FIG. 4 THEORETICAL CURRENT DISTRIBUTION $\epsilon_r = 0.5$ ($\omega = \sqrt{2}\ \omega p$), $k_0a = 0.04$ $b/a = 4$.

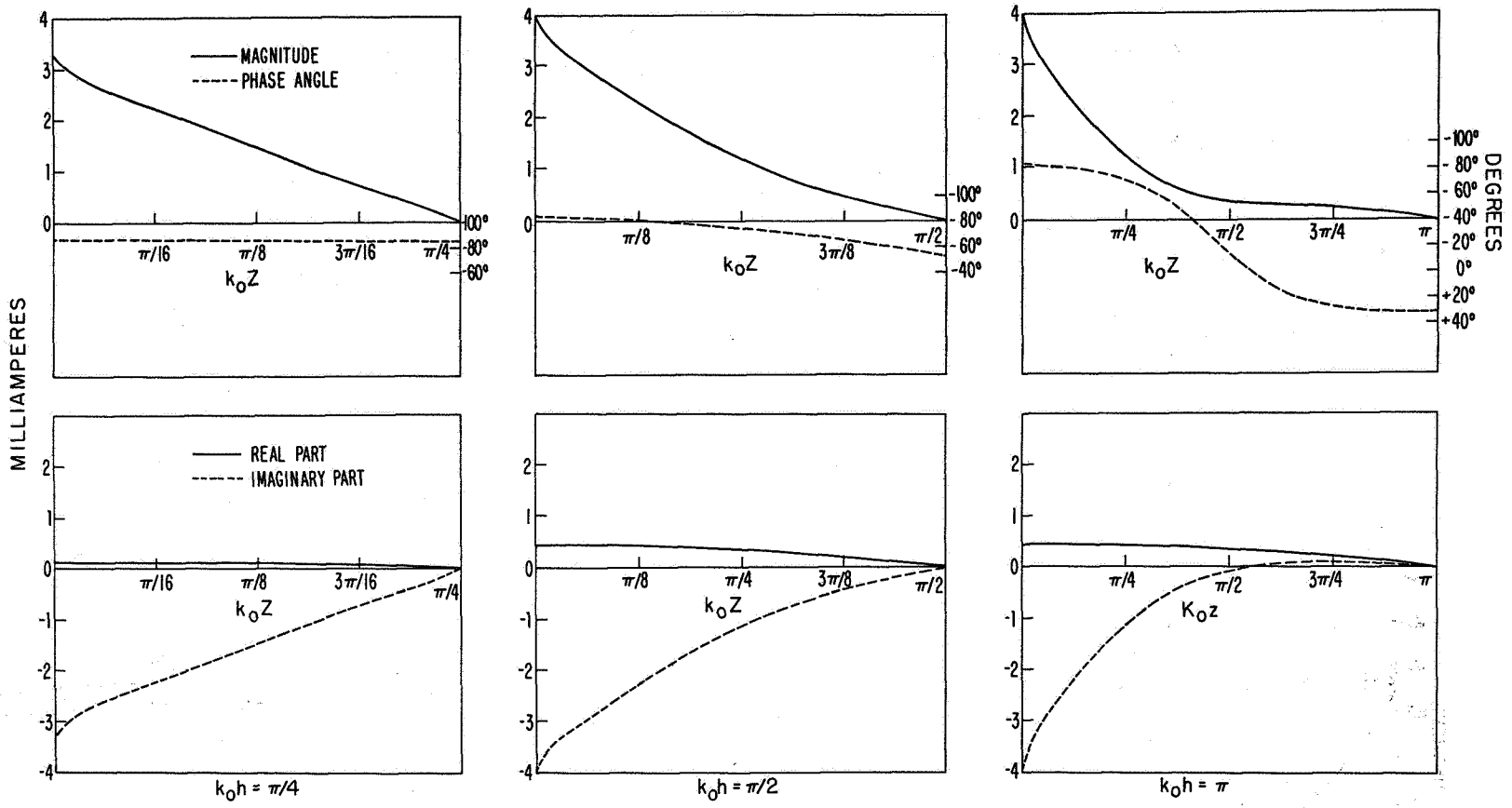

FIG. 5 THEORETICAL CURRENT DISTRIBUTION $\epsilon_r = -0.5$ ($\omega = \sqrt{2/3}\,\omega p$), $k_0a = 0.04$ $b/a = 4$.

the input admittance. Then, the input admittance as a function of antenna length of the two given cases is shown in Fig. 6. For the case $\epsilon_r = 0.5$, the curve becomes very broad, and the resonance peak is less sharp as compared with the free space dipole or the dielectric-coated dipole antenna. Since a delta-function driving source is assumed, theoretically the input susceptance should be infinitely capacitive. For an actual gap-driven antenna the curve of input susceptance should shift downward as in the case of the dielectric-coated one. For the case $\epsilon_r = -0.5$, the input conductance is very small. From theoretical consideration, the input conductance should be zero when the idealized plasma surrounding the antenna is unbounded. Owing to the finite diameter of the plasma column, there is a finite but small input conductance. The input susceptance is entirely inductive. This is because the current very close to the driving point, as given in [4], is

$$I(z \to 0) \sim -i 4 a \omega \epsilon_1 V \ell n\, z \tag{9}$$

With ϵ_1 negative, the infinite capacitance at the driving point becomes an infinite inductance. For an actual gap-driven antenna, the curve of input susceptance should shift upward. Also, it is noted that, since the current decays rapidly along the length of the antenna when the antenna is longer than a quarter-wavelength, the antenna begins to behave more like an infinite one with an input admittance that is almost constant and independent of the length.

D. Field Pattern

As derived in [2], by changing the cylindrical coordinates (r, θ, z) to spherical coordinates (R, Θ, Φ), and using the method of steepest descents, the far field is given by

$$\lim_{R\to\infty} B_\theta = \frac{e^{ik_0 R}}{2\pi^2 R} \left[\frac{-a\,\mu_0 I_0(aa)}{a\,b I_0(a\,b) H_1^{(1)}(Pb) - \epsilon_r Pb\, I_1(a\,b) H_0^{(1)}(Pb)} \right]_{x = -k_0 \cos\Theta} \int_{-h}^{h} I(z')\, e^{-ik_0 z' \cos\Theta}\, dz' \tag{10}$$

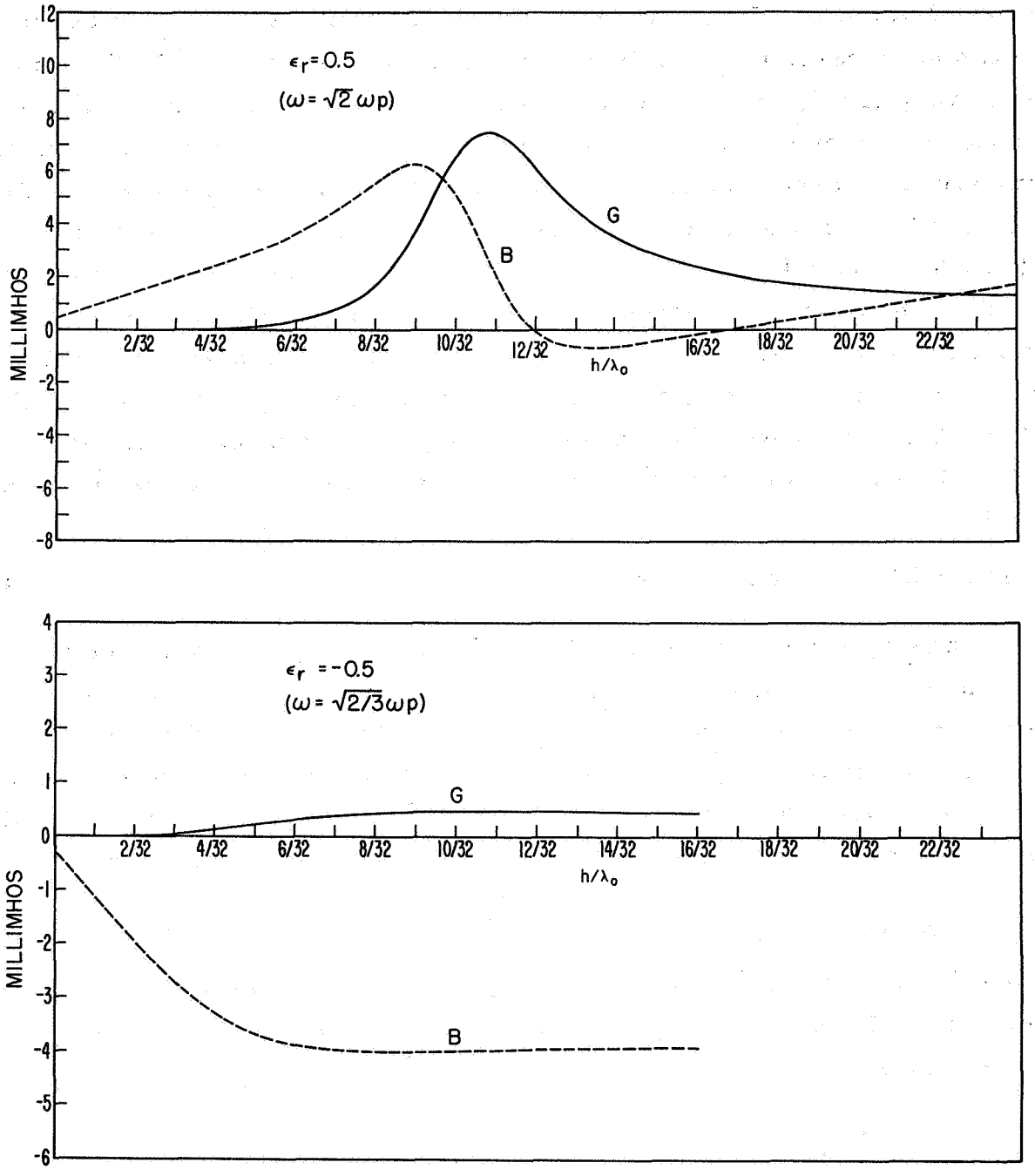

FIG. 6 THEORETICAL INPUT ADMITTANCE $G + iB$, $k_o a = 0.04$, $b/a = 4$

which can be calculated numerically from the numerical solution for $I(z)$ obtained before. The field factor $F_r(\Theta)$ is defined as

$$F(\Theta) = \frac{4\sqrt{15}\,\pi R}{\mu_0} \left| B_\theta \right| \tag{11}$$

The field pattern of (11) is shown graphically in Fig. 7 for $k_0 h = \pi/2$ and $k_0 h = \pi$. When $\epsilon_r = 0.5$, the field factor is quite large, and the shape of the pattern changes as the length of the antenna is increased. When $\epsilon_r = -0.5$, the field factor is much smaller, and the shape of the pattern (as in the case of a Hertz dipole) consists of two small circles which are almost independent of the length of the antenna. This is due to the fact that the main contribution to the radiation field comes from the current close to the driving point, since the current attenuates very rapidly along the length of the antenna.

E. Conclusions

The problem of a finite cylindrical antenna in an idealized plasma column has been solved by a numerical method for $\omega > \omega_p$ and for $\omega_p > \omega > \omega_p/\sqrt{2}$. The current distribution changes from an approximately sinusoidal function in the first case to an exponentially decaying function in the second case, and the far field changes from large values to very small ones with constant applied voltage. The case $\omega < \omega_p/\sqrt{2}$ is not discussed. Although the mathematics and the numerical method are the same as when $\omega_p > \omega > \omega_p/\sqrt{2}$, the plasma column can support a guided wave when $\epsilon_r < -1$, so that the Green's function has an extra residue contribution from a pole on the real axis. Because the plasma column encountered either in the laboratory or surrounding a vehicle is always of finite length, it would be necessary to take into account the reflections from the end of the column to obtain a satisfactory solution to the problem. This is likely to be difficult.

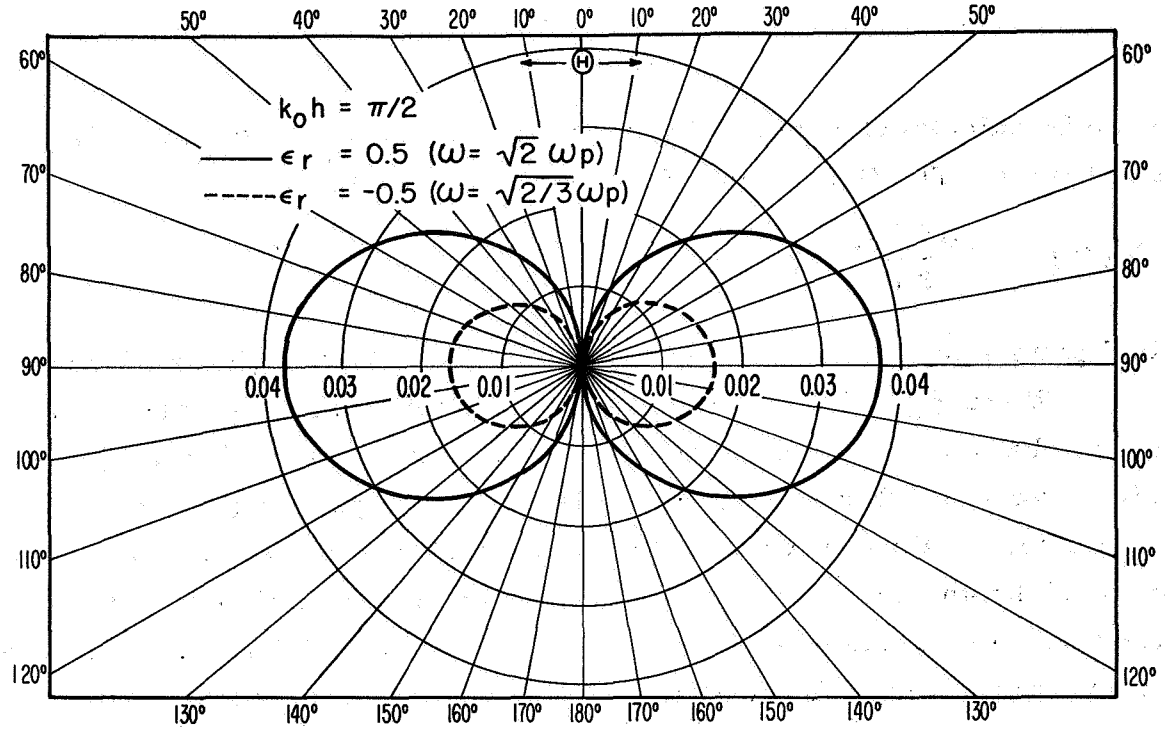

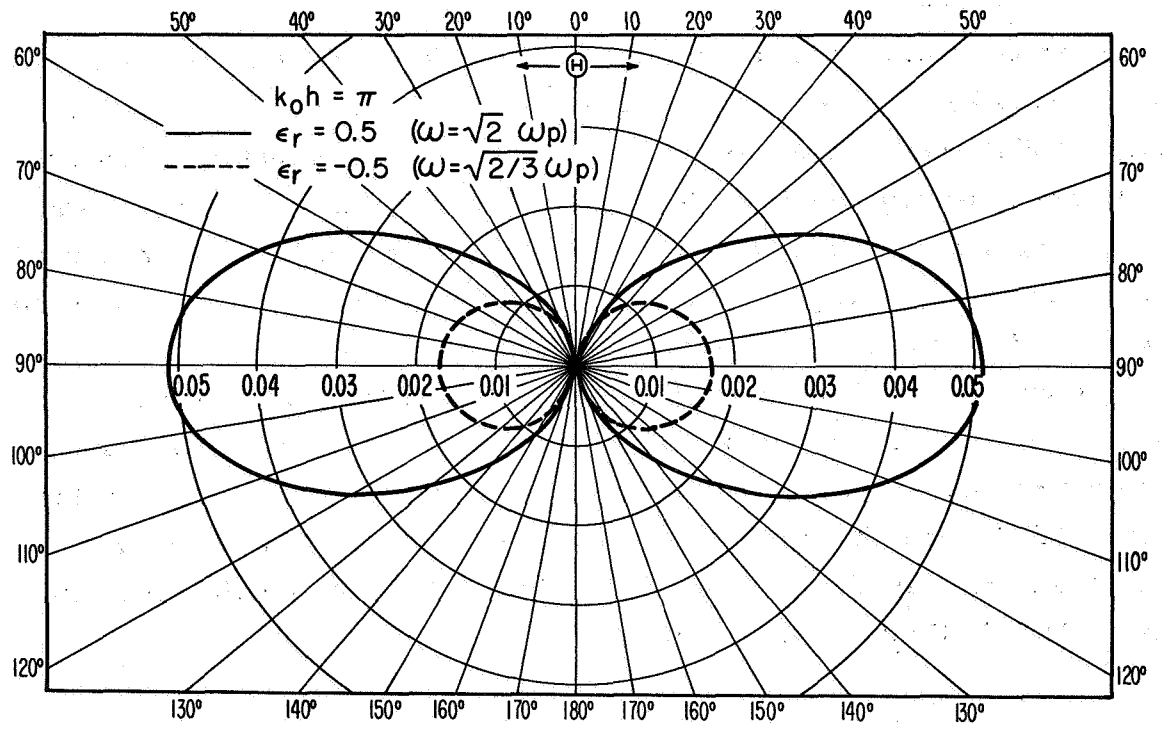

FIG. 7 FIELD PATTERNS $k_0a = 0.04$, $b/a = 4$

III. AN EXPERIMENTAL STUDY OF A PLASMA-COATED FINITE ANTENNA

A. Plasma Discharge Tube

The plasma sheath around the antenna was produced by means of a hot-cathode helium d.c. discharge contained within a long coaxial pyrex glass tube. As shown schematically in Fig. 8, the outer glass cylinder of the coaxial container had an inside diameter of 33 millimeters and a wall thickness of 2 millimeters; its length was 1.25 meters (about 2.5 wavelengths in air at the operating frequency of 600 megacycles per second). The diameter of the inside glass tube was 9 millimeters; its wall thickness, 1 millimeter; and its length, 0.55 meter. The pyrex glass had a relative dielectric constant of $\epsilon_r = 4.8$ and loss tangent $\tan\delta = 0.004$. The inner glass tube served as a d.c. insulating sleeve around the antenna, so that no d.c. current was drawn from the discharge by the antenna. It was thus possible to avoid complicated d.c. rectification effects within the plasma due to the presence of the metallic antenna. A matrix type Semicon cathode was mounted at the end of the discharge tube away from the antenna. The anode consisted of a thin molybdenum strip placed concentrically around the coaxial line and mounted flush with respect to an aluminum ground plane. This arrangement ensured that the antenna was always located inside the positive column of the plasma discharge. The plasma container was placed perpendicular to the aluminum ground plane and was supported by a block of polyfoam. Figure 11 shows a picture of the discharge tube in operation mounted in front of the ground plane. The aluminum ground plane was approximately 7 ft x 6 ft. It was used to screen electrically the plasma-antenna assembly from the vacuum equipment and measuring apparatus which were installed directly behind it. To minimize the reflection from the surrounding objects, the entire antenna assembly was placed inside a microwave anechoic chamber.

The plasma tube could be pumped down to pressure as low as 10^{-7} mm Hg with a model 3305 NRC oil diffusion pump. The high vacuum pressures were monitored by an NRC-type 720B Phillips ionization gauge. To prevent contamination and out-gassing during the course of the experiment, the plasma container was baked out for several hours at 450° C during the cathode conversion process

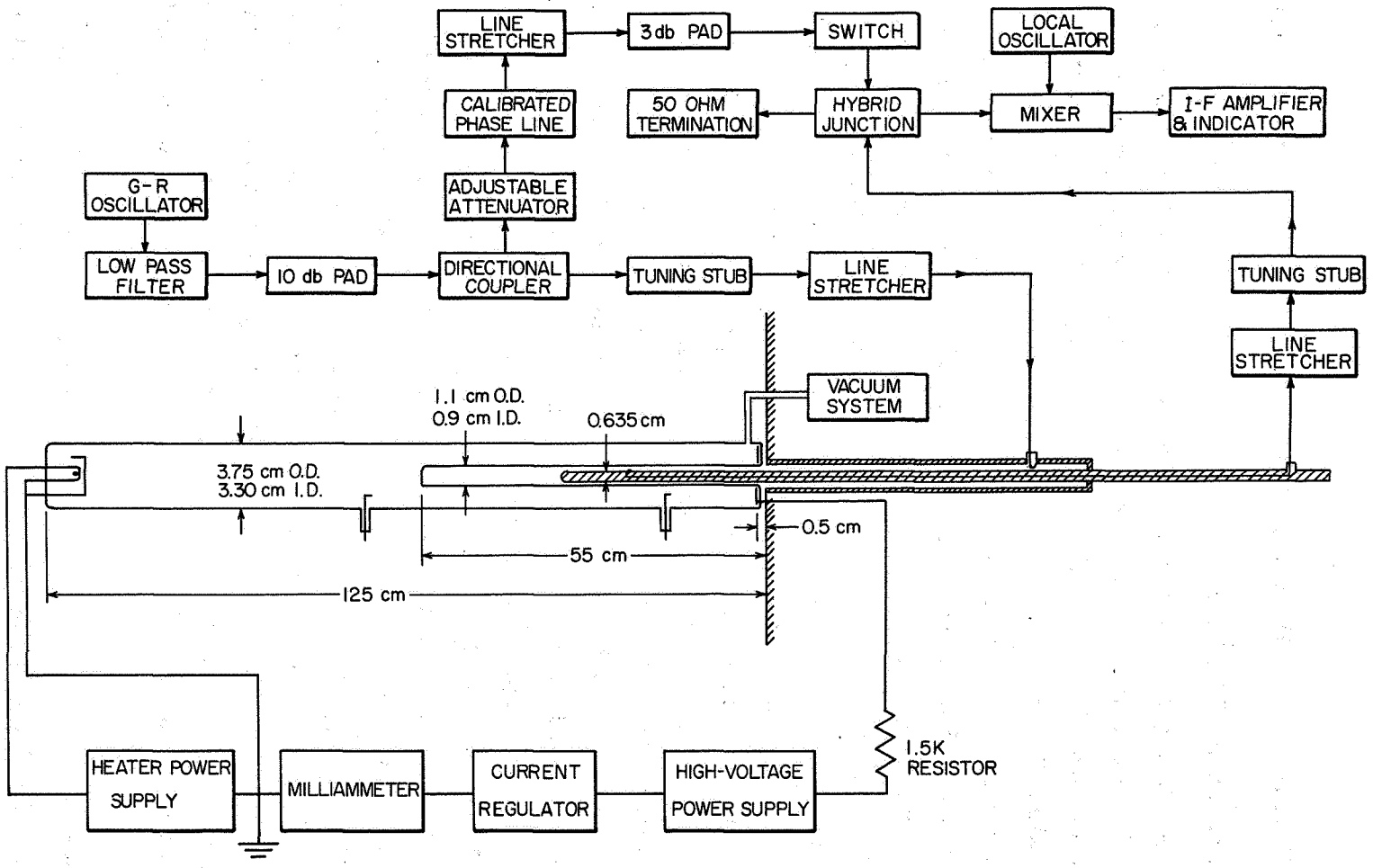

FIG. 8 SCHEMATIC SKETCH OF EXPERIMENTAL APPARATUS FOR ANTENNA MEASUREMENTS

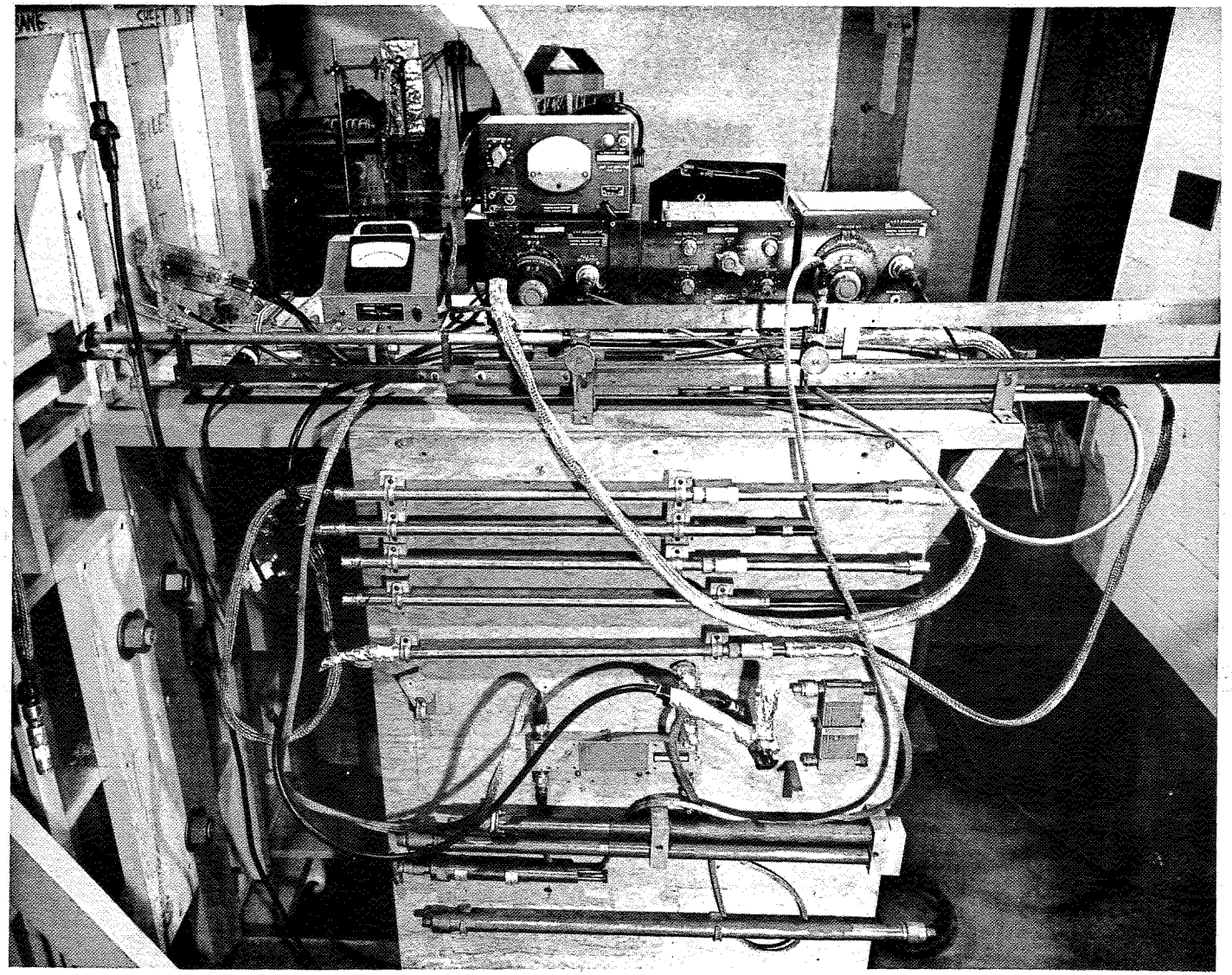

FIG. 9 PICTURE OF THE APPARATUS FOR ANTENNA MEASUREMENTS

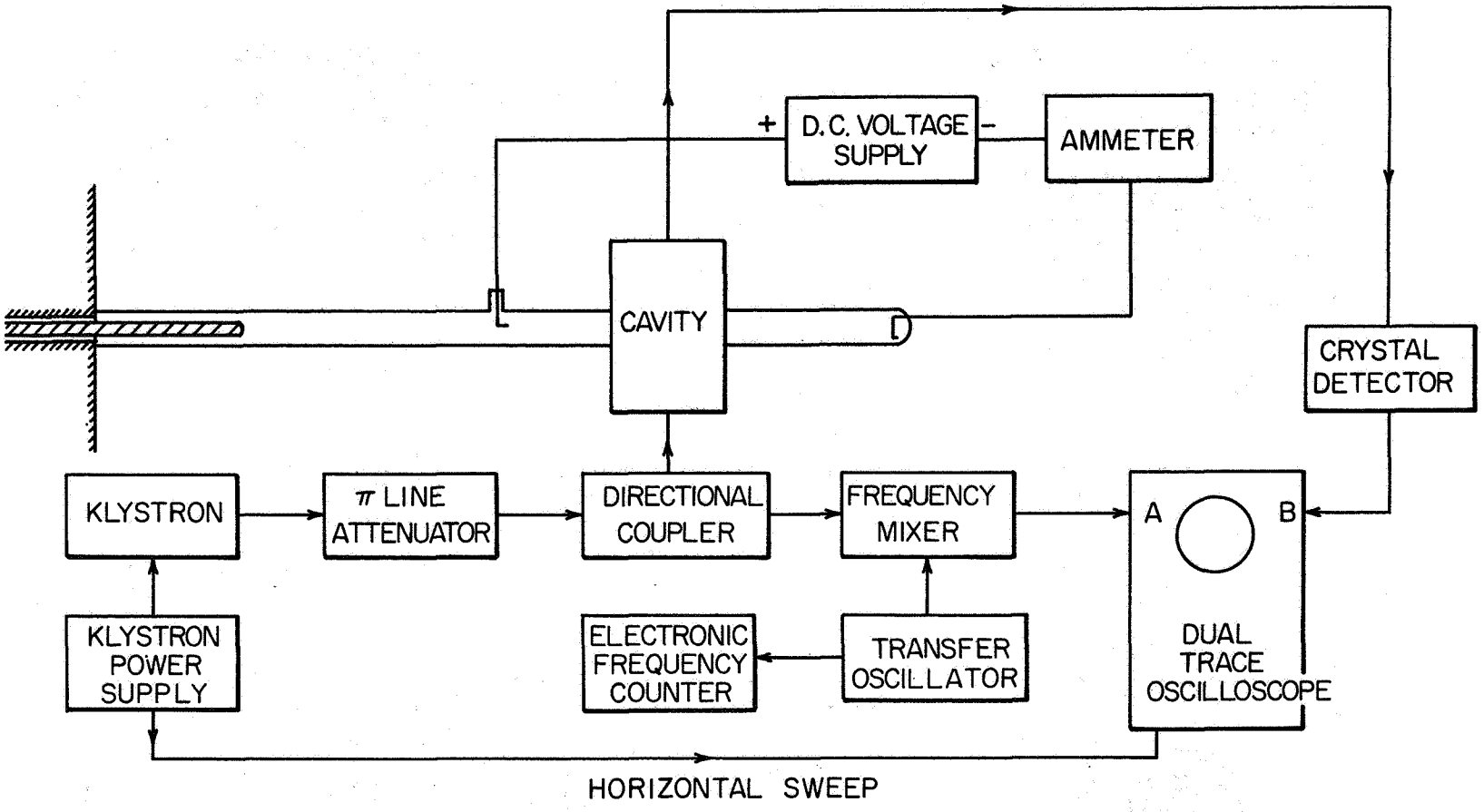

FIG. 10 BLOCK DIAGRAM OF EXPERIMENTAL SET UP FOR PLASMA DIAGNOSTICS, SINGLE LANGUMIR PROBE AND CAVITY PERTURBATION TECHNIQUES

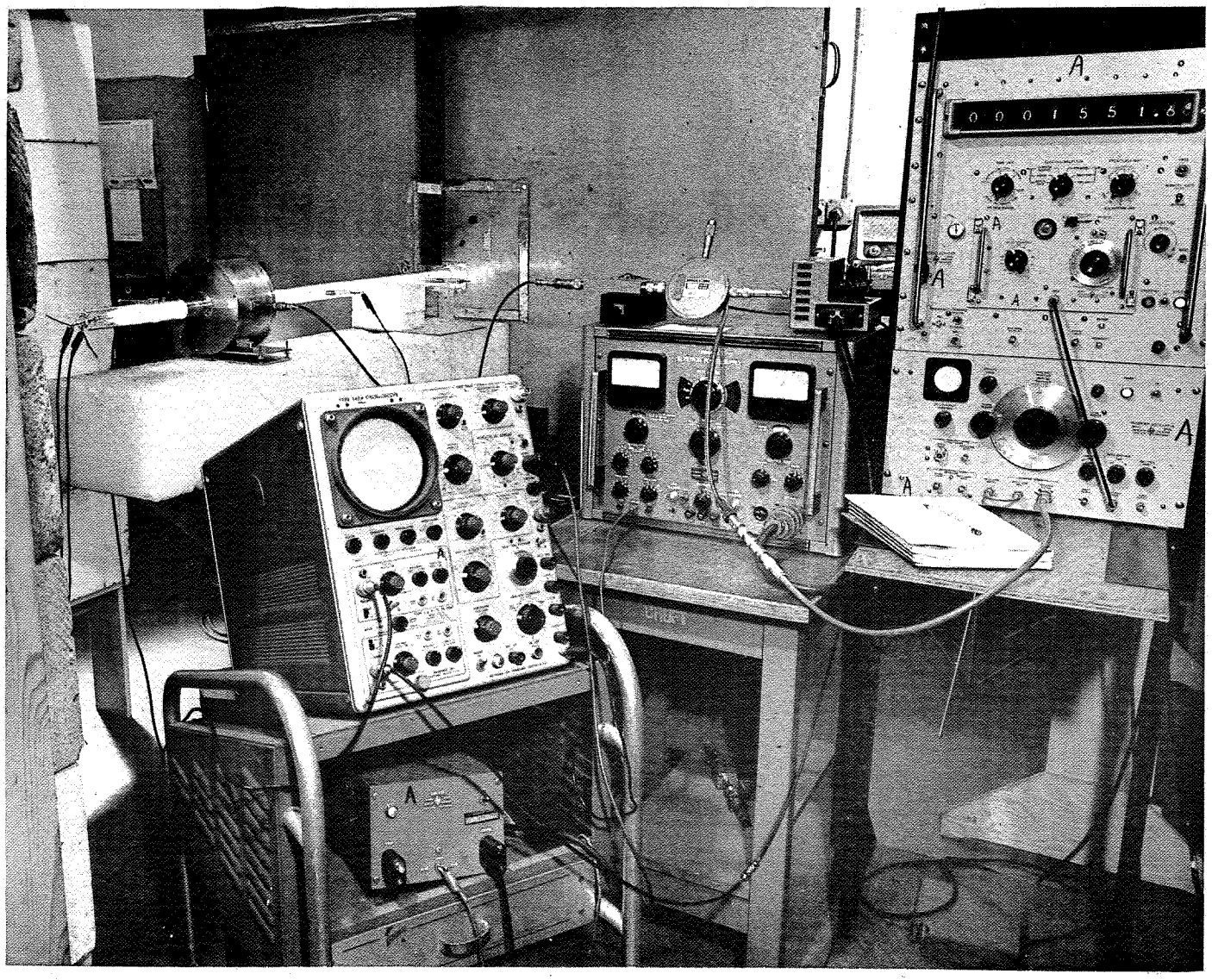

FIG. 11 PICTURE OF THE APPARATUS FOR PLASMA DIAGNOSTICS

and also at periodic intervals later on as the need arose. After a pump-down pressure of 10^{-7} mm Hg was obtained, the plasma container was sealed off from the vacuuam system by a bakeable Granville-Phillips valve. To avoid the possibility of the oil from the diffusion pump leaking into the discharge tube, a liquid nitrogen cold trap was always used in series with the plasma tube during pumping. The discharge tube was then back-filled with helium (reagent-type gas, 99.9 percent pure) to any desired pressure by means of a low torque type-C Granville-Phillips valve. The pressure inside the discharge tube could be monitored by a Hastings DV-16 thermocouple gauge. The pressure of the helium gas as well as the d.c. discharge current through the tube could be varied over a wide range. Typical values of pressure varied from 0.05 to 1.0 torr of Hg; the d.c. discharge current varied from 30 to 270 ma. Typical operating d.c. anode voltages were around 500 to 700 volts, with a 1500-ohm (200 watt) current-limiting resistor in series. During the course of the experiment, the d.c. discharge current was held constant by a Kepco model CK-60 0.5M constant current regulator connected in series with the high voltage supply. The maximum range of electron densities obtainable from this type of discharge tube varied from 10^{9} to 10^{11} electrons per cm^{3}, corresponding to plasma frequencies between 280 to 2800 MHz. Because the operating frequency of the antenna was 600 MHz, investigations could be made both above and below, as well as in the immediate vicinity of the plasma frequency where the most interesting plasma effects manifest themselves. The electron temperature of the plasma discharge varied from 40,000 ^{o}K (5.2 electron volts) to about 70,000 ^{o}K (9.1 electron volts). To minimize the effect of contaminants and to facilitate reproducible date, the discharge tube was completely flushed out and pumped down to 10^{-7} mm Hg before each experiment. The Semicon cathode was operated at 1000 to 1050 ^{o}C; the cathode temperature was monitored by an optical pyrometer. About 30 watts of heater power were required for these optimum cathode temperatures.

To facilitate the measurement of the electron densities and electron temperatures, two cylindrical single Langmuir probes were mounted inside the discharge tube—one close to the antenna and the other further down the tube

nearer to the cathode. To obtain a measurement of the electron density and the effective collision frequency by an independent method, the cavity perturbation method was used. A cylindrical cavity is mounted on the tube in the region of positive column near the cathode as shown in Figs. 10 and 11. The diagnostic techniques are described in detail in Section II-C

B. Antenna Assembly

The antenna was the center conductor of a coaxial line which could be extended beyond an aluminum ground plane into the inner glass sleeve of the plasma container. The antenna was made from 1/4 - in diameter brass tubing; its length could be varied from 0 to 30 cm by means of a rack and pinion arrangement. The outer conductor of the coaxial line driving the antenna was made from 9/16 - in brass tubing. The characteristic impedance of the coaxial line was 48.6 ohms. A 1/16 - in wide slot was cut along the entire length of the antenna; through this slot projected a shielded loop probe which was used to measure the amplitude and phase of the current along the antenna. The probe, approximately 2.5 millimeters in diameter, was fabricated from a precision coaxial tube of 0.021-in outer diameter and 0.003-in wall thickness. It was mounted on a 3/16 - in diameter brass tubing, which slid inside the antenna tubing. It could be set at any desired position along the antenna by means of another rack and pinion arrangement. The signal picked up by the probe was carried to the detector by a microdot cable. From the coaxial line, R F power was fed to the antenna by a T-shaped shunt connected to the main line at a distance of about a quarter-wavelength from the short-circuited end. A rough cross-sectional view of the antenna assembly is shown in Fig. 8.

C. Plasma Diagnostic Measurements

The plasma diagnostic measurements were made with two basically different d.c. and microwave measuring techniques. The single Langmuir probe method [5] (d.c. measurement), which has been used for over 40 years, provides information about the electron density and electron temperature. The cavity

perturbation method (microwave measurement) provides information about the electron density and effective collision frequency. A brief description of each of these methods is given below.

Two cylindrical Langmuir probes were used. One was mounted in the discharge tube near the antenna, the second nearer the cathode. The Langmuir probes were each 3 millimeters long and were made from 0.005 - in diameter tungsten wire. The position of the probe could be varied over the cross section of the discharge tube by means of a magnetic slug. The electron temperature and density were determined from the probe current-voltage characteristics [5]. A typical characteristic curve is shown in Fig. 12. The electron temperature was determined from the slope of the curve from the formula

$$\frac{d(\ell n\, i_e)}{dV_p} = - \frac{1.17 \times 10^4}{T_e} \tag{12}$$

where i_e is the electron probe current, T_e is the electron temperature in degrees Kelvin, and V_p is the probe potential in volts with respect to the anode. The electron density η_0 is given by the equation

$$\eta_0 = \frac{i_{ep}}{A\sqrt{T_e}} \times 4.018 \times 10^9 \quad \text{electrons/cm}^3 \tag{13}$$

where $A = 2\pi rh$ is the area in square meters, r is the radius, and h is the length of the Langmuir probe; i_{ep} is the electron current in amperes at the plasma potential, and T_e is the electron temperature in degrees Kelvin.

The electron density and the electron temperatures measure by the Langmuir probe near the cathode at the center of the positive column for various pressures and discharge currents are shown in Figs. 13 and 15. The corresponding plasma frequency is shown in Fig. 14. In general, the electron density as well as the plasma frequency increase with increasing discharge current or pressure. For a pressure of 300 microns, the electron density ranges from 1.24×10^4 electrons per cm^3 at a discharge current of 40 ma to 5.06×10^{10} electrons per cm^3 at discharge current of 180 ma. The corresponding plasma frequency ranges from 1.05 gigacycles per second to 2.02 gigacycles per second. The electron temperature as shown in Fig. 15 is near

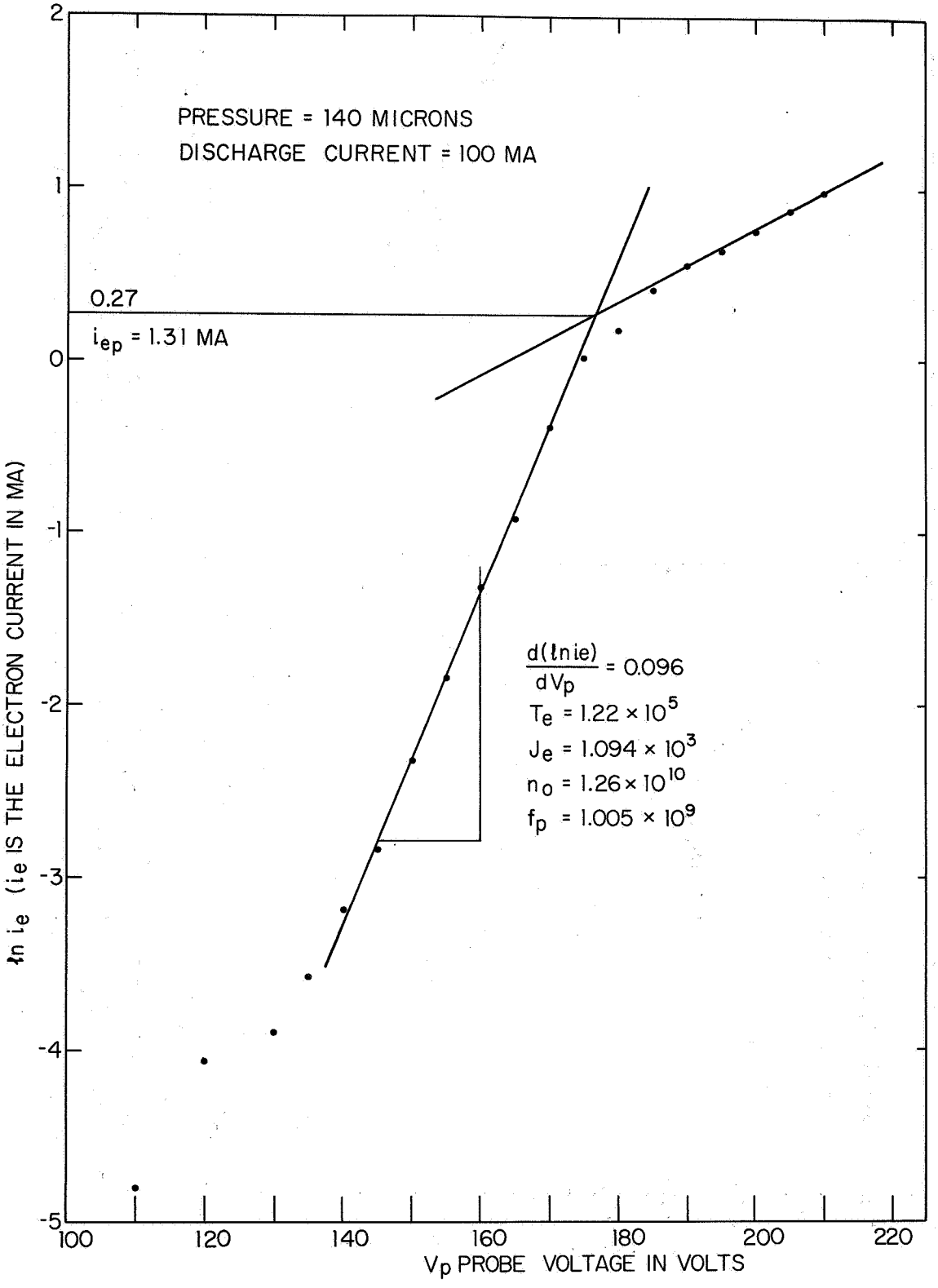

FIG. 12 CHARACTERISTIC CURVE OF ELECTRON CURRENT VS APPLIED VOLTAGE OF A SINGLE LANGMUIR PROBE

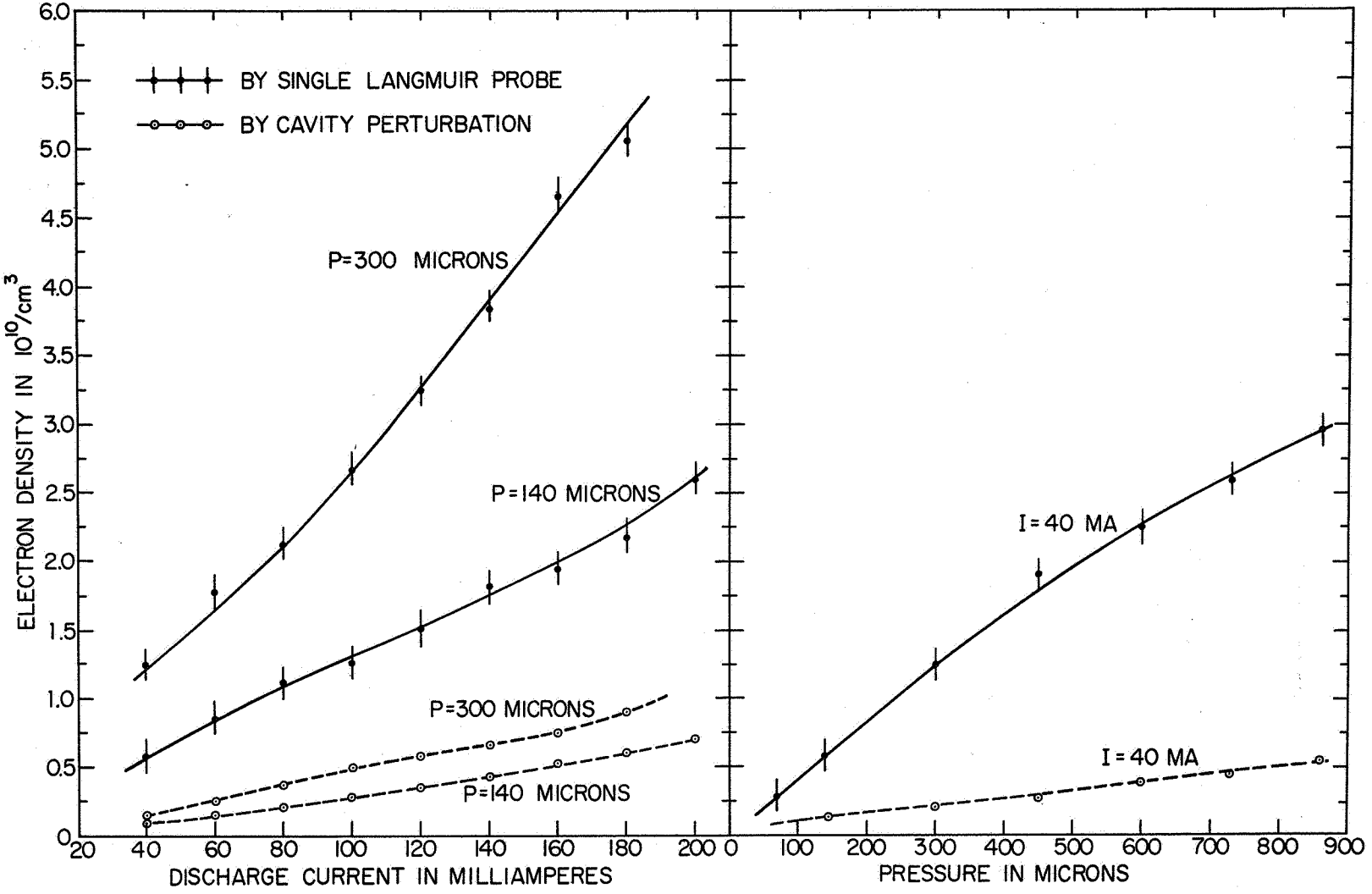

FIG. 13 MEASURED ELECTRON DENSITY AS A FUNCTION OF DISCHARGE CURRENT AND PRESSURE

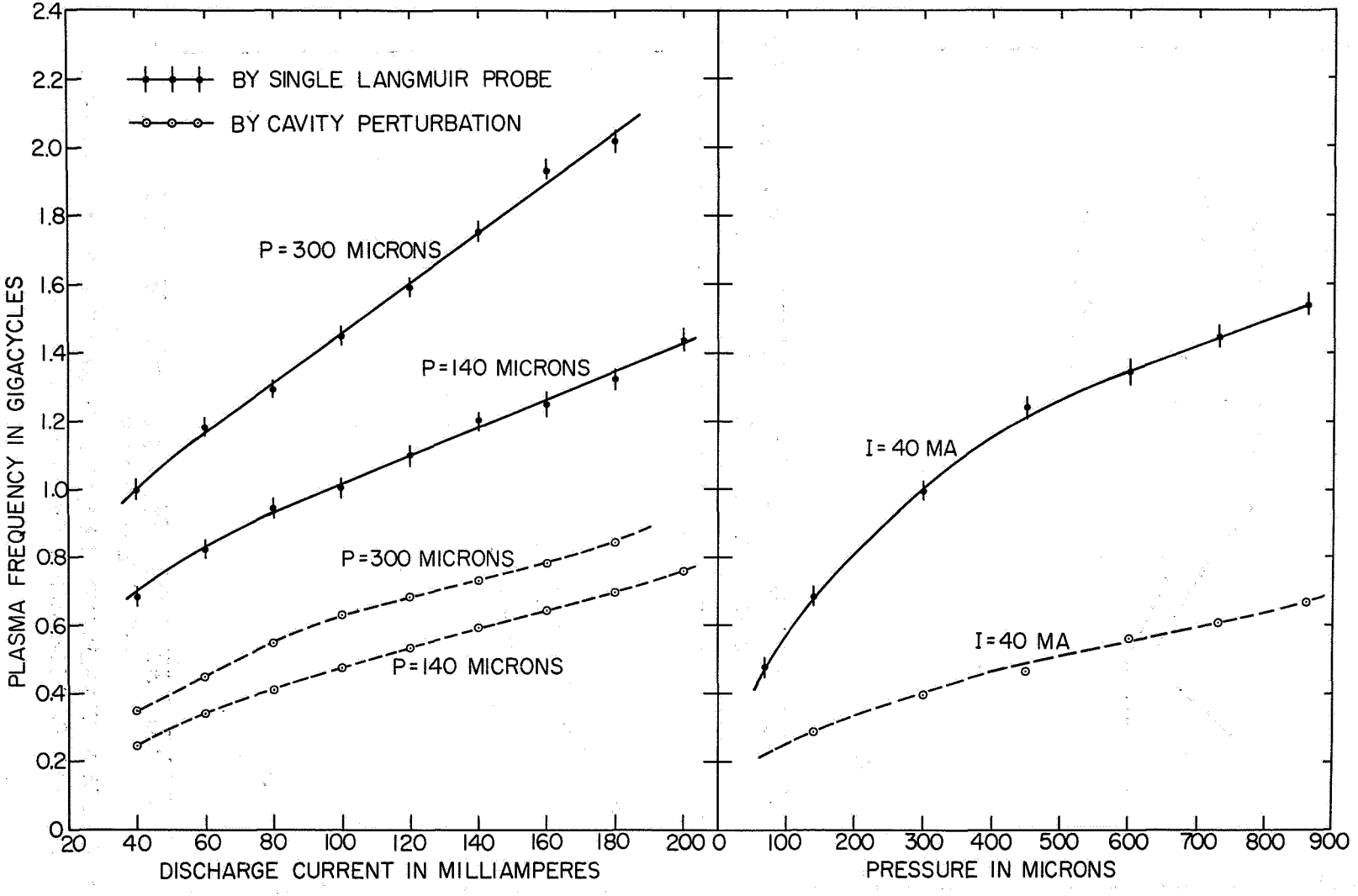

FIG. 14 MEASURED PLASMA FREQUENCY AS A FUNCTION OF DISCHARGE CURRENT AND PRESSURE

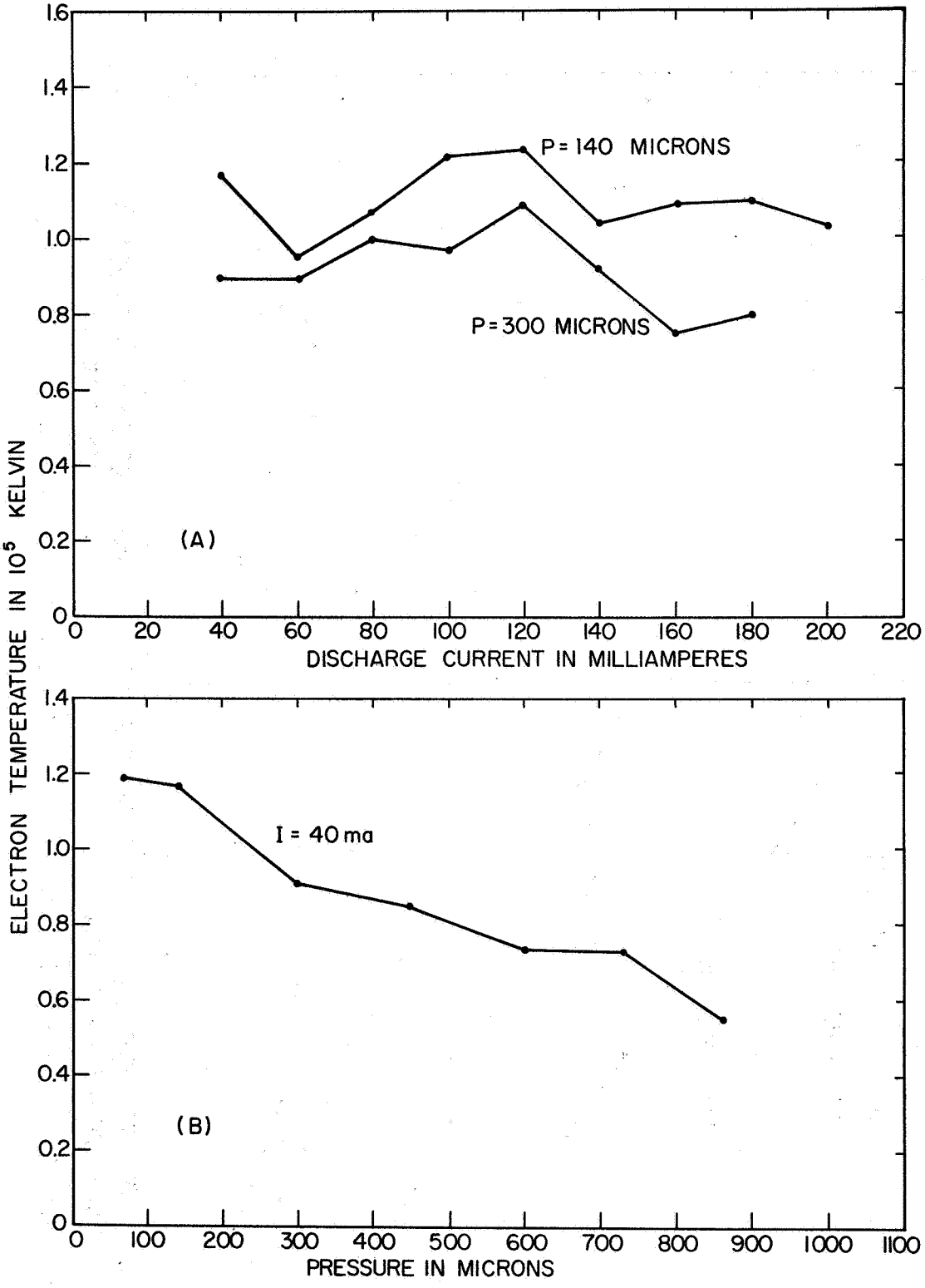

FIG. 15 ELECTRON TEMPERATURE MEASURED BY SINGLE LANGMUIR PROBE AS FUNCTION OF DISCHARGE CURRENT AND PRESSURE

10^5 °K. It shows that the electron temperature is more dependent on the pressure than on the discharge current—the higher the pressure, the lower the electron temperature.

The Langmuir probe method is based on the Maxwellian distribution law. However, for low pressure-high energy plasmas, the Maxwellian distribution becomes somewhat questionable. Also, the presence of the probe in the plasma disturbs the plasma, especially when the probe voltage is much lower or higher than the plasma in its vicinity. Moreover, there is always much uncertainty in drawing two straight lines (such as those shown in Fig. 12) to determine i_{ep}. As a consequence, the measured electron density and temperature are likely to be in error.

The electron density measured by the second Langmuir probe very close to the antenna shows that the electron density in that coaxial tube region does not have circumferential symmetry. Because of the pinch effect, the electron beam always tends to be concentrated on one side of the coaxial tube. This can be observed when a magnet is placed close to the tube and the plasma sheath moves from one side to the other. The measurement shows that the electron density is higher than that measured by the first probe when the second probe is in the higher density region and becomes extremely low when it is in the lower density region. If the number of electrons per unit length were the same along the tube, the average electron density in the coaxial region should be 1.125 higher than in the single tube region.

The microwave-cavity perturbation method for studying plasmas has been described by S. C. Brown and others[6]. It consists mainly in observing the change in resonant frequency and the lowering of the Q of the resonant cavity when it is partially filled with plasma. For low plasma densities ($\omega_p^2 << \omega^2$) and low collision rates ($\nu << \omega$), and by assuming that the collision frequency is uniform across the tube, the peak electron density η_0 at center of the tube and the angular collision frequency can be determined from the following two equations:

$$\eta_0 = \left(1 + \frac{\nu^2}{\omega^2}\right) \quad 8\pi^2 \left(\frac{m\varepsilon_0}{e^2}\right) f_0 \ \Delta f \ \frac{1}{F(r_p, r_0, h)} \tag{14}$$

$$\nu = \frac{\pi f_0^2 \left(\frac{1}{Q_p} - \frac{1}{Q_0}\right)}{\Delta f} \tag{15}$$

where m and e are the mass and charge of the electron, f_0 is the resonance frequency of the unperturbed cavity, Δf is the resonance frequency shift due to the presence of the plasma column. $F(r_p, r_c, h)$ is a function of the mode excited in the cavity, the dimensions of the cavity and the plasma column and the electron density profile inside the plasma column. It is given by

$$F(r_p, r_c, h) = \frac{\int_0^{r_p} \int_0^{2\pi} \int_0^{h} \eta(r) E^2(r, \theta, z) r \, dr \, d\theta \, dz}{\int_0^{r_c} \int_0^{2\pi} \int_0^{h} E^2(r, \theta, z) r \, dr \, d\theta \, dz} \tag{16}$$

where $\eta(r)$ is the electron density profile function, $E(r, \theta, z)$ is the electric field distribution of the approximate mode excited in the cavity, and r_p, r_c and h are respectively the inside radius of the plasma tube, the radius of the cavity and the height of the cavity. The electron profile distribution commonly used in this type of measurement is the Schottky diffusion profile of the type $J_0(2.404\, r/r_p)$ [5]. However, this profile distribution is valid only at fairly high pressures when the mean free path is small compared to the radius of the plasma column; the profile is limited by ambipolar diffusion in this case. As the pressure is lowered, the gas-kinetic collisional frequency is too low to set up diffusion, and the electron density profile shows marked deviation [7]; the profile seems to become more uniform across the cross section of the tube. Significant errors can result, if the Schottky profile function is used for calculating electron densities at lower pressures (for helium this has been observed when the pressure is lower than 140 microns). A multimode cavity perturbation scheme

has been devised by Ramo Rao [8] to extend the plasma diagnostics to lower pressures. In his forthcoming technical report, the profile function is expanded as a power series of the normalized radius r/r_p and the profile coefficients are evaluated by measuring the shift in the resonance frequencies of the appropriately chosen cavity modes.

The S-band microwave cavity used in the measurement was a right circular cylinder 11.272 cm in diameter and 11.43 cm in length. It was of the transmission type, and energy was coupled in and out of the cavity by means of small loop probes. Two circular cylinders approximately 2 inches long and with the same radius as the plasma tube were attached to the end faces of the cavity. These sections acted like waveguides beyond cutoff and helped to improve the Q of the cavity. The plasma tube was placed at the center of the cavity along its axis. The modes which have been carefully identified and used in the measurement were the TM_{020}, TM_{120}, and TE_{212}. The cavity was tuned individually to each of these modes, and the frequency shift of each mode was measured with the plasma present and absent. The $F(r_p, r_c, h)$ functions for the TM_{020} and TM_{120} modes and for the geometrical dimensions of the experimental model are given by

$$F_{120}(r_p, r_c, h) = \frac{\dfrac{r_p^2}{2.405}\, J(2.405) - \dfrac{(5.520)^2}{2r_0^2}\, r_p^4 \left\{\dfrac{1}{4} - \dfrac{(2.405)}{24} + \dfrac{1}{16}\dfrac{(2.405)^4}{32}\right\}}{\dfrac{r_c^2}{2}\, J_1^2(5.520)}$$

$$= 0.113 \qquad (17)$$

$$F_{120}(r_p, r_c, h) = \frac{\left(\dfrac{7.016}{2r_c}\right)^2 r_p^4 \left[\dfrac{1}{4} - \dfrac{1}{4}\dfrac{(2.405)^2}{6} + \dfrac{1}{64}\dfrac{(2.405)^4}{8}\, r_p^4\right]}{\dfrac{r_c^2}{2}\left[J_1^2(7.016) - J_0(7.016)\, J_2(7.016)\right]}$$

$$= 2.419 \times 10^{-2} \qquad (18)$$

The accuracy of the cavity technique was checked by replacing the plasma column by a dielectric rod having a known dielectric constant. The measured value of the dielectric constant was within 5 percent error.

Figure 10 shows the experimental setup used for the plasma diagnostic measurements. A swept frequency signal from a klystron generator was fed to the cavity. A synchronous d.c. voltage was used as the horizontal sweep of the oscilloscope, so that both the resonance curve of the cavity and the mode curve of the klystron appeared simultaneously on the screen of a dual trace oscilloscope. The frequency shifts could be measured with an accuracy of better than 0.01 MHz with a Hewlett Packard model 524C electronic digital counter in conjunction with an ultrastable transfer oscillator and harmonic generator model 540B. The resonance frequencies of the modes TM_{020}, TM_{120}, TM_{210}, TE_{212} were 2.9065, 3.8184, 2.8249, and 3.0982 GHz . The TM_{020} (J_0 - type field distribution) produced large frequency shifts, and TM_{210} (J_2 - type field distribution) produced very small shifts. The TM_{120} and TE_{212} produced intermediate frequency shifts. Typical frequency shifts for the TM_{020} mode varied from 0.56 MHz at a pressure of 50 microns to 8.70 MHz at a pressure of 8.60 microns for a constant discharge current of 40 ma. The corresponding frequency shift for the TM_{120} mode varied from 0.10 to 1.10 MHz . For the TM_{210} mode the frequency shift varied from 0.04 megacycles at a pressure of 140 microns to 0.14 MHz at a pressure of 860 microns for the same discharge current.

The measured results for the electron density and the plasma frequency at the center of the tube are shown in Figs. 13 and 14. The TM_{020} mode was used for the constant pressure curve P = 140 microns; and the TM_{120} mode was used for the constant pressure curve P = 300 microns. Both TM_{020} and TM_{120} modes were used for the constant discharge current curve I = 40 ma. Results are quite close. The curve shown in Figs. 13 and 14 is the result of the TM_{020} mode. In all these measurements, Schottky's profile has been used. The effective collision frequency measured in the TE_{212} mode is shown in Fig. 16. It can be seen that the collision losses become quite significant at higher pressures. For example, at a pressure of 800 microns the collision

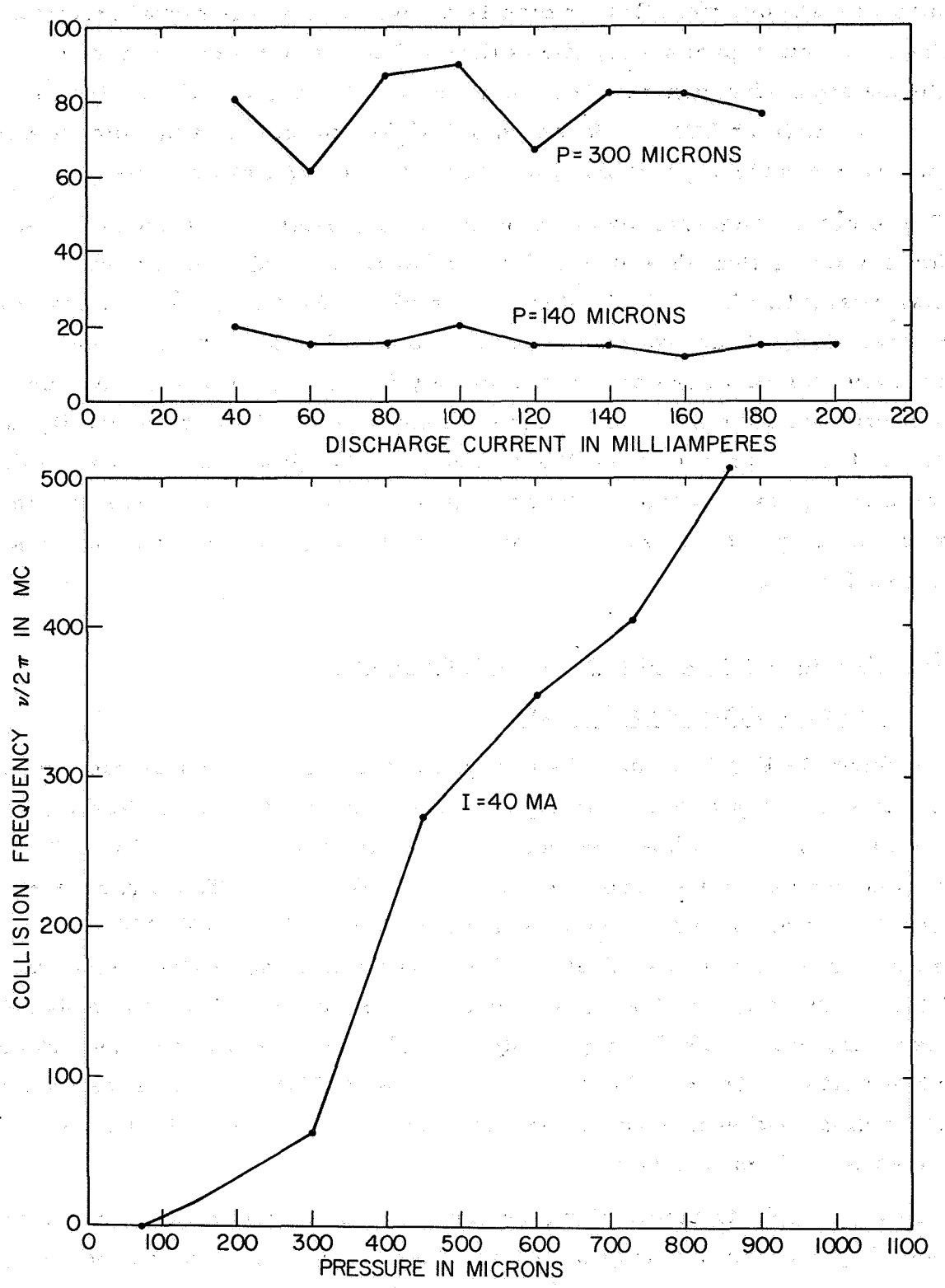

FIG. 16 COLLISION FREQUENCY MEASURED BY THE CAVITY PERTURBATION METHOD AS FUNCTION OF THE DISCHARGE CURRENT AND PRESSURE

frequency was almost 500 MHz , which is comparable to the signal frequency of 600 MHz . At lower pressures, the collision frequency becomes quite low compared to the signal frequency. For example, at 140 microns the collision frequency was only 15 MHz . Hence, most of the antenna measurements were made at low pressures, principally at 140 microns and 300 microns.

The electron density measured by the cavity perturbation technique is considerably lower than that obtained in the Langmuir probe measurements. A similar result has been obtained by Levitskii and Sashurin [9], who made a comparative study of the two diagnostic methods. Errors in the cavity measurement can also result from inaccuracy in the choice of the electron density profile function, from the fringing of the electric field in the cavity near the holes in the end plates, from the presence of the glass tube, and sometimes from too large a perturbation. The calculation of the effective collision frequancy is based upon the assumption that it is radially independent, but this is not necessarily true.

D. Measurement of Current Distribution and Input Admittance of the Antenna

As shown in Fig. 8, a superheterodyne detecting system was used in the experimental investigations. The signal generator was a General Radio (GR) 1361-A unit oscillator with a frequency range from 450 to 1050 MHz . The maximum power output was approximately 200 milliwatts. The higher harmonics generated by the oscillator were suppressed by a GR 874-F 1000 low-pass filter with a cutoff frequency of 1000 MHz . The detecting system consisted of a GR 1216-A, 30 MHz , I.F. amplifier used in conjunction with a GR 874-MR mixer rectifier with a IN21B crystal diode. The local oscillator was another GR 1361-A unit oscillator. The I.F. amplifier was calibrated with the sinusoidal voltage distribution in a short-circuited coaxial line. A pictorial view of the apparatus is given by Fig. 9.

The current distribution along the antenna can be completely described by measuring the relative amplitude and phase. The amplitude of the current can be measured easily with the output of the shielded loop probe fed directly

into the detecting system. To measure the relative phase of the antenna current, the signal from the probe was compared with a reference sampling signal obtained from the main signal generator by means of a directional coupler. The amplitude and phase of the reference signal could be varied by a GR calibrated coaxial attenuator and a line stretcher. The probe and the reference signal were mixed in a coaxial hybrid junction and the difference arm of the hybrid was connected to a detecting system. By adjusting the phase and amplitude of the reference signal, a minimum indication could be obtained in the detector, signifying that the probe signal and the reference signal were 180° out of phase. After establishing such a reference point, the phase of the current at other points along the antenna could be determined with respect to it by noting the setting of the line-stretcher in the reference arm which gave a minimum indication in the detector.

The input admittance of the antenna was determined by measuring the standing-wave ratio and the position of the current minimum in the coaxial line driving the antenna [10]. The terminal function of the antenna load was calculated from the formula

$$\rho_s = \coth^{-1} S \tag{19}$$

where S is the current standing-wave ratio. The apparant phase function of the load can be found from the equation

$$\Phi_s = \frac{\pi}{2} + \beta (\omega_1 - \omega_2) \tag{20}$$

where $\beta = {}^{2\pi}/_{\lambda g}$ is the phase constant of the coaxial line and ω_1 is the position of the current minimum with a short circuit terminating the line, and ω_2 is the position of the current minimum with the antenna load. The input admittance of the antenna $G + jB$ was then calculated from the formulas

$$\frac{G}{Y_c} = \frac{\sinh 2\rho}{\cosh 2\rho + \cos 2\Phi} \tag{21}$$

$$\frac{B}{Y_c} = \frac{\sin 2\Phi}{\cosh 2\rho + \cos 2\Phi} \tag{22}$$

where Y_c is the characteristic admittance of the coaxial line.

The current distribution of quarter-wavelength and half-wavelength monopoles and the input admittances of the monopoles of varying lengths were measured for various gas pressures and discharge currents at an operating frequency of 600 MHz . Figure 17 shows the current distributions along a quarter-wavelength monopole for different pressures or discharge currents in the order of increasing plasma frequency. Figure 18 shows the change of the current distribution along a half-wave monopole as the discharge current increases at a constant pressure of 140 microns. Figure 19 shows the current distribution in the half-wave monopole at a constant pressure of 300 microns. Figure 20 shows the change of the current distribution along a half-wave monopole as the pressure increases with a fixed discharge current of 40 ma. All of these curves of current distribution are normalized to the measured input admittances. Among the measured curves of input admittances as functions of antenna length, eight were selected and are shown in Fig. 21. These are lettered alphabetically in the order of increasing plasma frequency. It gives a clear picture of how the input admittance curve changes as the plasma frequency increases.

E. Discussion of the Experimental and Theoretical Results

The aim of the experiments described in this report is to examine the influence of a plasma sheath on the near-field properties of an insulated cylindrical antenna, principally its current distribution and input admittance. Ideally, it would be desirable to generate a homogeneous, lossless, cold plasma column of infinite length to correspond to the simplified theoretical model postulated in Section II. In reality, however, practical limitations are such that it was possible to produce a plasma column only a few wavelengths long. The electron-density profile across the plasma tube was diffusion controlled and far from uniform; the electron temperature was very high, and the losses due to collisions were considerable, especially at high pressures. It was also necessary to produce the plasma inside a glass container so that glass walls and an air gap were interposed between the antenna and the plasma sheath. Furthermore, measurements of the electron density by the Langmuir

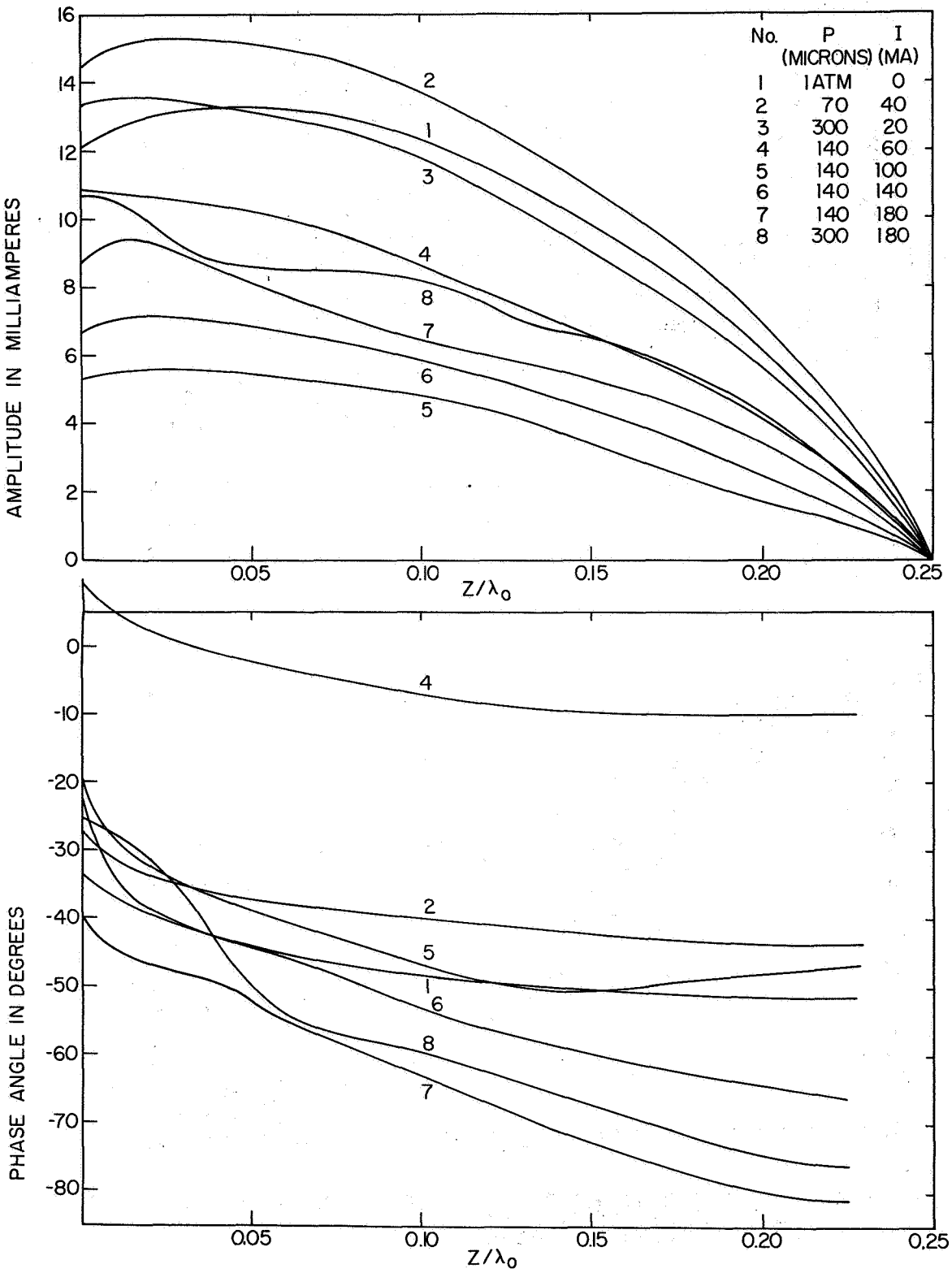

FIG. 17 MEASURED CURRENT DISTRIBUTION OF A QUARTER-WAVELENGTH MONOPOLE FOR VARIOUS PRESSURE P AND DISCHARGE CURRENT I

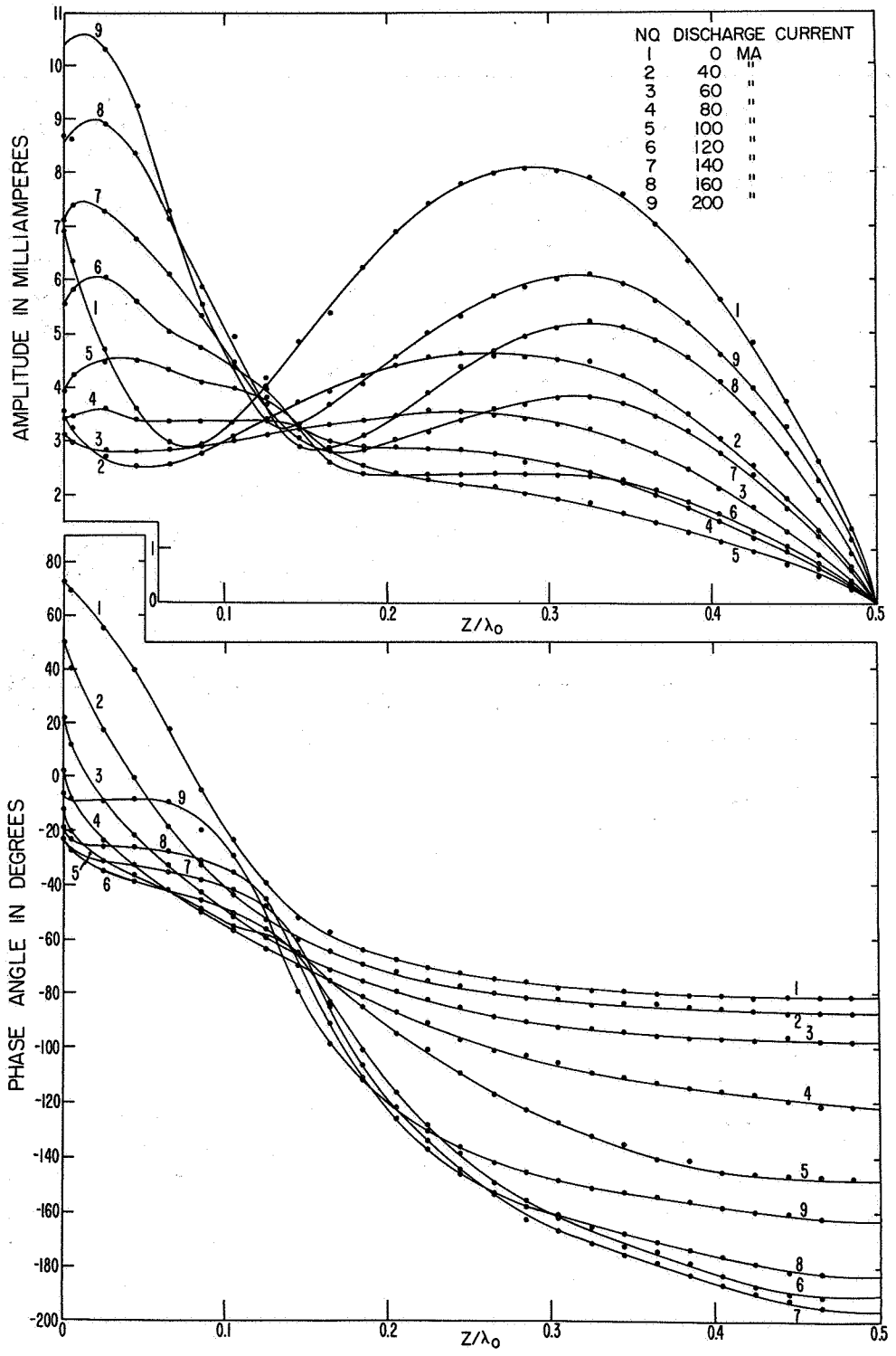

FIG. 18 MEASURED CURRENT DISTRIBUTION OF A HALF-WAVELENGTH MONOPOLE WITH DISCHARGE CURRENT AS PARAMETER
PRESSURE = 140 MICRONS GAS=HELIUM

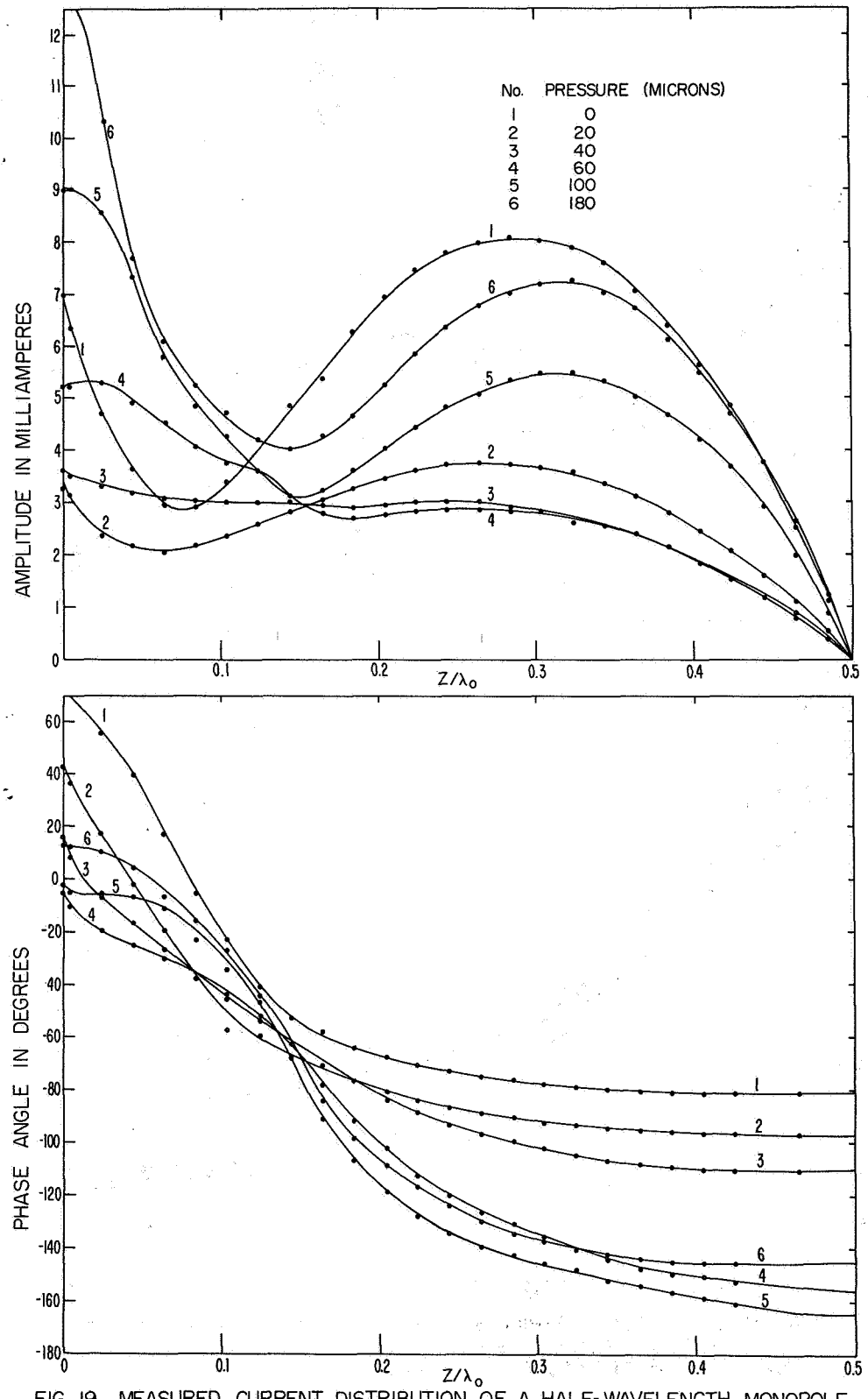

FIG. 19 MEASURED CURRENT DISTRIBUTION OF A HALF-WAVELENGTH MONOPOLE WITH DISCHARGE CURRENT AS PARAMETER
PRESSURE = 300 MICRONS GAS = HELIUM

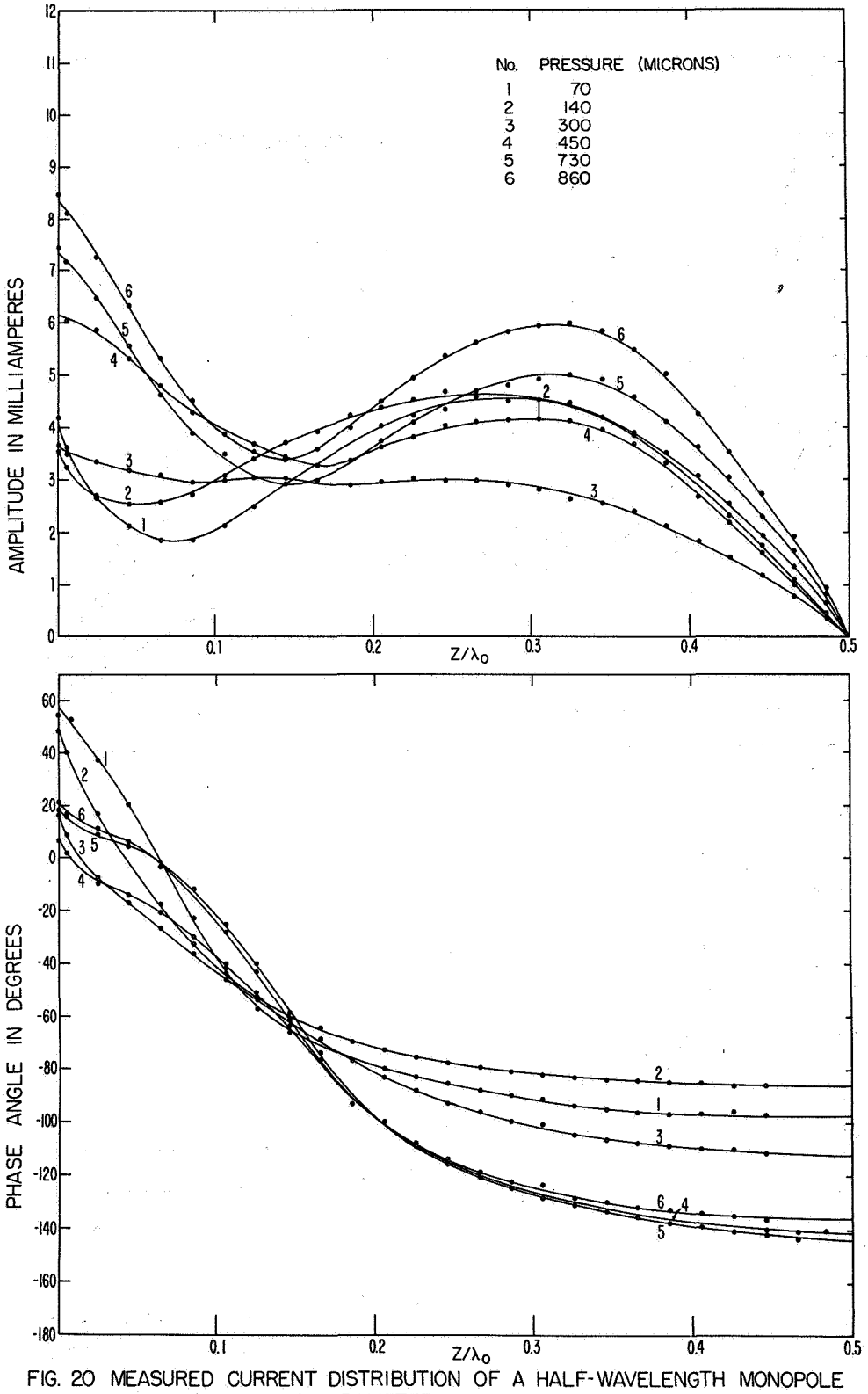

FIG. 20 MEASURED CURRENT DISTRIBUTION OF A HALF-WAVELENGTH MONOPOLE WITH PRESSURE AS PARAMETER
DISCHARGE CURRENT = 40 MA GAS = HELIUM

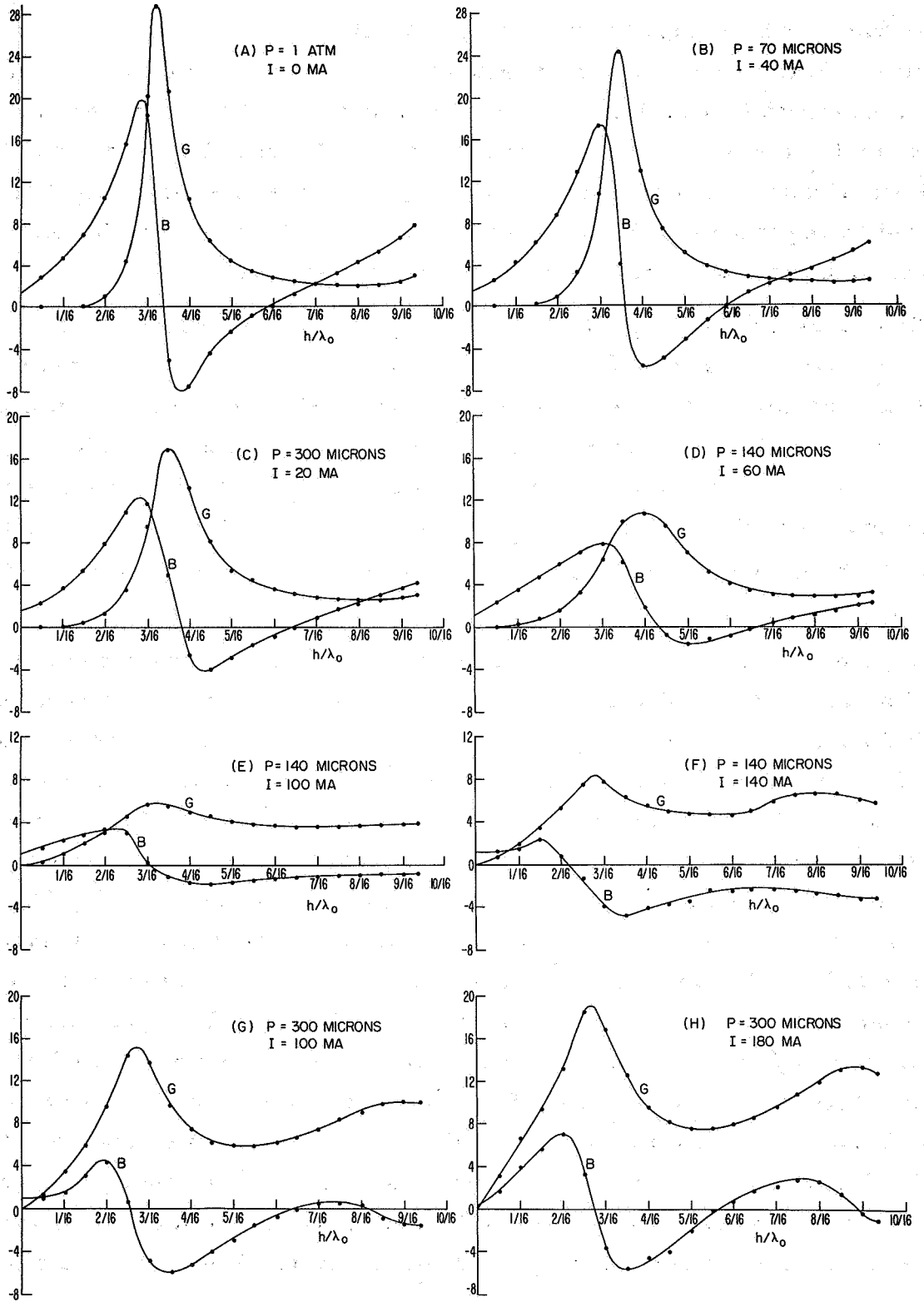

FIG. 21 MEASURED INPUT ADMITTANCE G + iB IN MILLIMHOS VS ANTENNA LENGTH

probe near the antenna show that the plasma in the annular region around the antenna does not have angular symmetry. All these effects have not been taken into account in the theoretical calculations. In view of these practical limitations a meaningful, quantitative comparison of the predicted, theoretical results and the measured, experimental data is difficult. Nevertheless, this experimental work was undertaken in the hope that the most significant features predicted by the theory could be observed, and a qualitative correlation between the theoretical and experimental results could be achieved.

Qualitatively speaking, the significant properties predicted by the theory can be summarized as follows. First, for $\omega > \omega_p$, the plasma acts as a dielectric medium, and the effect of the presence of the plasma sheath is to shorten the effective electrical length of the antenna. And secondly, for $\omega_p > \omega > \omega_p/\sqrt{2}$, the plasma sheath tends to attenuate the current along the antenna and the radiated field. Thirdly, for $\omega_p > \omega > \omega_p/\sqrt{2}$ when the antenna is longer than quarter-wavelength; it behaves very much like an infinitely long one.

Figure 17 shows the current distribution on a quarter-wavelength monopole. The current distribution for this length of the antenna is not as sensitive to variations in the plasma frequency as that in a half-wave monopole. Curve 1 shows the current distribution without plasma. Curves 2, 3, and 4 show the effect of shortening the electrical length of the antenna as the plasma frequency increases. Curves 5, 6, 7, and 8 show some interesting new features which will be discussed later. The most interesting set of curves is in Fig. 18, which shows the current distribution of a half-wavelength monopole at a constant pressure of 140 microns, but varying discharge currents ranging from 0 to 200 milliamperes. Curve 1 is the current distribution without plasma, which is very similar to that for an antenna in air. Because of the presence of the two dielectric layers of the glass tube, the antenna behaves as if it were electrically slightly longer than when in air. For a discharge current of 40 ma, as shown by curve 2, the plasma frequency is much lower than the operating frequency. It clearly indicates the shifting of the minimum towards the left. This means that the effective length of the antenna is now shorter. The amplitude of the

current decreases sharply due to the collision losses. These phenomena become even more pronounced for a discharge current of 60 ma as shown by curve 3. Curve 4 is near the critical region. The plasma frequency, at least in part of the tube, must be close to the operating frequency. The general shape looks like that of a quarter-wavelength monopole in air. However, other peaks begin to appear. As the plasma frequency increases further, a new kind of standing wave appears in the distribution curve of the antenna current. Its wavelength is shorter than the wavelength in air, and its amplitude attenuates rapidly along the antenna. The theory predicts this attenuation for $\omega < \omega_p$, but not the standing-wave type of distribution observed in the experiment, since the glass-air gas has been ignored in the theoretical analysis. The exploration for the standing-wave phenomenon is as follows.

In a plasma medium with collisions, when the plasma frequency is higher than the operating frequency, the plasma acts like a lossy conducting medium in the sense that it reflects waves which are incident upon it. The antenna structure shown in Fig. 8 indicates that when the plasma becomes a lossy conducting medium, then the composite antenna-plasma system behaves like a coaxial line filled with two types of dielectric layers, namely, the glass wall and the air gap. For an approximate estimation for the wave propagating along such a structure, the plasma medium is replaced by a perfect conductor, as shown in Fig. 22. Assume the wave propagates along the z-axis with propagation constant k, then the dispersion relation of the structure can be found easily. It is given by the equation

$$\xi \left[J_0(\xi b) Y_0(\xi c) - J_0(\xi c) Y_0(\xi b) \right] \left[I_1(\beta b) K_0(\beta a) + I_0(\beta a) K_1(\beta b) \right]$$

$$- \varepsilon_r \beta \left[J_1(\xi b) Y_0(\xi c) - J_0(\xi c) Y_0(\xi b) \right] \left[I_0(\beta b) Y_0(\beta a) - I_0(\beta a) K_1(\beta b) \right] = 0 \tag{23}$$

where $\beta = \sqrt{k^2 - k_0^2}$, $\xi = \sqrt{k_1^2 - k^2}$, $k_0 = \omega\sqrt{\mu_0 \varepsilon_0}$, $k_1 = \sqrt{\varepsilon_r} k_0$, and a, b, c are defined in Fig. 22. Use of the numerical values shown in Fig. 8, namely, $2a = 0.635$ cm, $2b = 0.9$ cm, $2c = 1.1$ cm, $\varepsilon_r = 4.8$, gives for the propagation constant k calculated by a computer $k/k_0 = 1.23616$. The corresponding wavelength $2\pi/k$ is slightly longer than the distance between

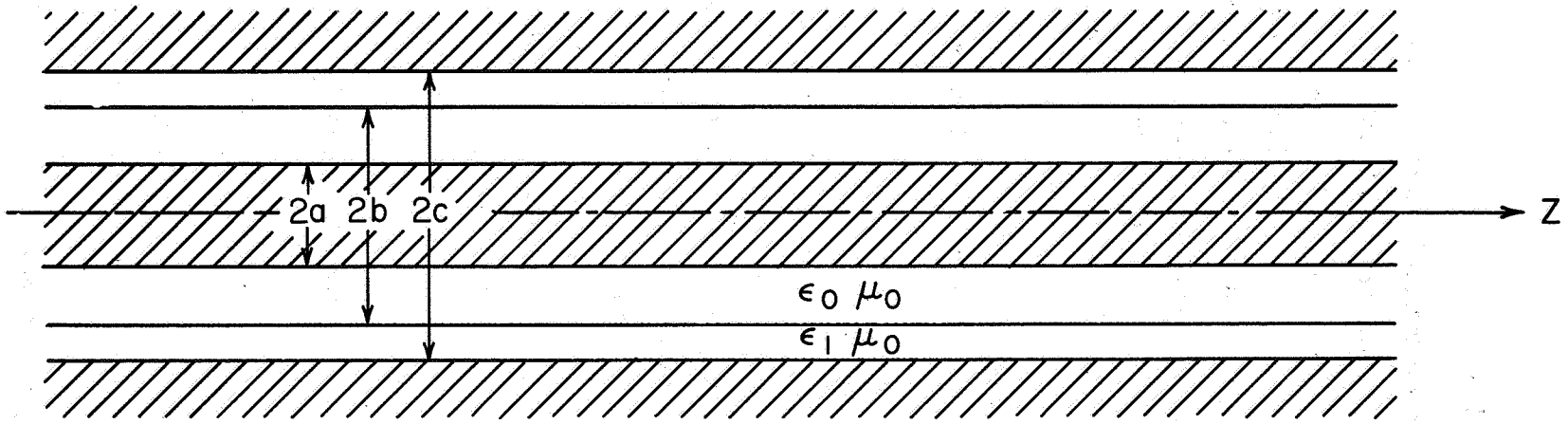

FIG. 22 A SCHEMATIC DIAGRAM OF AN INFINITE COAXIAL LINE FILLED WITH TWO LAYERS OF DIELECTRICS

the minimum point of the magnitude of the current and the end of the antenna, this is similar to the current distribution along a dipole in air in terms of true wavelength in air. As the discharge current increases, the reflectivity of the plasma becomes better; the standing wave also becomes sharper, as indicated by curves 6, 7, 8, and 9. Figure 19 shows the antenna currents at the higher pressure of 300 microns. The currents vary in the same manner explained before, but the collision losses are slightly higher in this case. Figure 20 shows the variation in current distribution for a fixed discharge current of 40 milliamperes and for increasing pressures. The curves have essentially the same variation with increasing pressure.

In Fig. 21, eight selected curves of the input admittance as a function of the antenna length have been shown in the order of increasing plasma frequency. They show vividly the change of the input admittance curve as the plasma frequency increases. For case A, without the plasma, the admittance curve is almost the same as that of a dipole in air. In case B, the plasma frequency is much lower than the operating frequency. The resonance peak shifts toward the right, and the magnitude of the peak is reduced as predicted by the theory. As the plasma frequency goes higher, the phenomena becomes even more obvious as shown by curves C and D. Note that the shape of the curve in D is almost the same that of the theoretical curve shown in Fig. 6 for $\epsilon_r = 0.5$. In E, the plasma frequency is in the vicinity of the operating frequency or slightly above it. The curve is now much broader. When the antenna is longer than a quarter-wavelength, it begins to behave like one that is infinitely long, as has been predicted theoretically for the case $\omega_p > \omega > \omega_p/\sqrt{2}$. As the electron density increases, the coaxial line mode of the wave forms along the antenna. The input admittance is again sensitive to the length of the antenna beyond a quarter-wavelength. The resonance due to this coaxial line mode becomes sharper as the electron density goes higher as indicated by curves F, G, and H.

From the measured curves of the current distributions and input admittances, it seems that the electron density measured by the cavity perturbation techniques is more reasonable than that measured by a single Langmuir probe.

F. The Resonance Behavior of a Short Monopole in a Plasma Column

In the absence of the plasma column, a short dipole antenna is predominantly capacitive, with a very small resistive component. It is also well known that a variable electric field $Ee^{j\omega t}$ in a plasma causes an equivalent displacement current $\vec{J}_e = \vec{E}\, G_0 (1 - \omega_p^2/\omega^2)(j\omega - \nu)$, which lags in place with respect to the electric field in the range $\omega < \omega_p$, and thus can be regarded formally as an inductive current. If the electron-neutral collision losses are also taken into account, the body of the plasma essentially behaves like a lossy inductive sleeve around the antenna. A simplified quasi-static equivalent circuit of the antenna-plasma system is, then, a parallel-resonant circuit consisting of the antenna capacitance in parallel with the lossy inductive component due to the plasma. At antiresonance, the rf current on the antenna decreases sharply and is accompanied by a corresponding increase in the input resistance of the antenna. The Q at resonance is, of course, proportional to ω/ν where ν is the electron-neutral collision frequency. In Fig. 23 the measured input resistance and reactance of a short monopole antenna ($h = \lambda_0/16$) is shown as a function of the d.c. discharge current. The measurements were made at three different pressures, 300 μ, 140 μ, and 70 μ, to demonstrate the effect of the collision losses on the effective Q of the resonant system. It can be seen from these curves that the antenna displays a behavior of the antiresonant type. The measured input resistance is a maximum for certain values of the discharge current whose corresponding plasma frequency is slightly higher than the operating frequency as predicted in order to make the plasma an inductive element, while the input reactance shows an abrupt antiresonant type of transition in this region. The input reactance does not, however, vanish at antiresonance because of the complicated nature of the equivalent circuit of the antenna-plasma system. It is also seen from these curves that the Q of the resonance curve is sharper at lower pressure when collision losses are correspondingly smaller. To confirm this resonance phenomenon, the approximately $1/r^2$ Coulomb-type field near the antenna was measured by means of a small receiving probe mounted inside the discharge close to the antenna. The receiving electric probe was oriented to pick up the E_z component

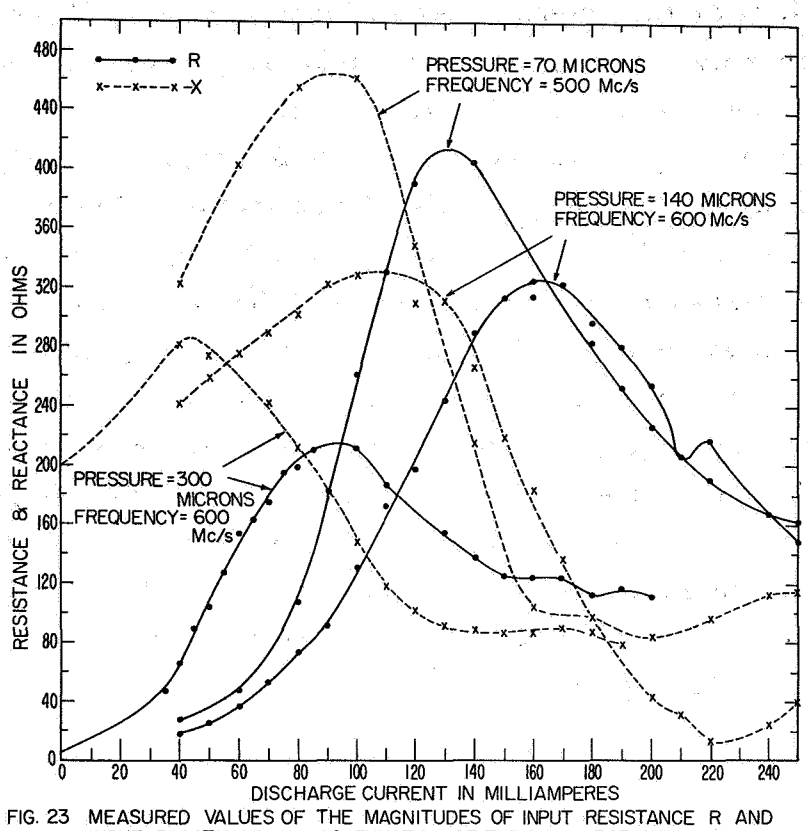

FIG. 23 MEASURED VALUES OF THE MAGNITUDES OF INPUT RESISTANCE R AND INPUT REACTANCE -X AS FUNCTION OF THE DISCHARGE CURRENT.

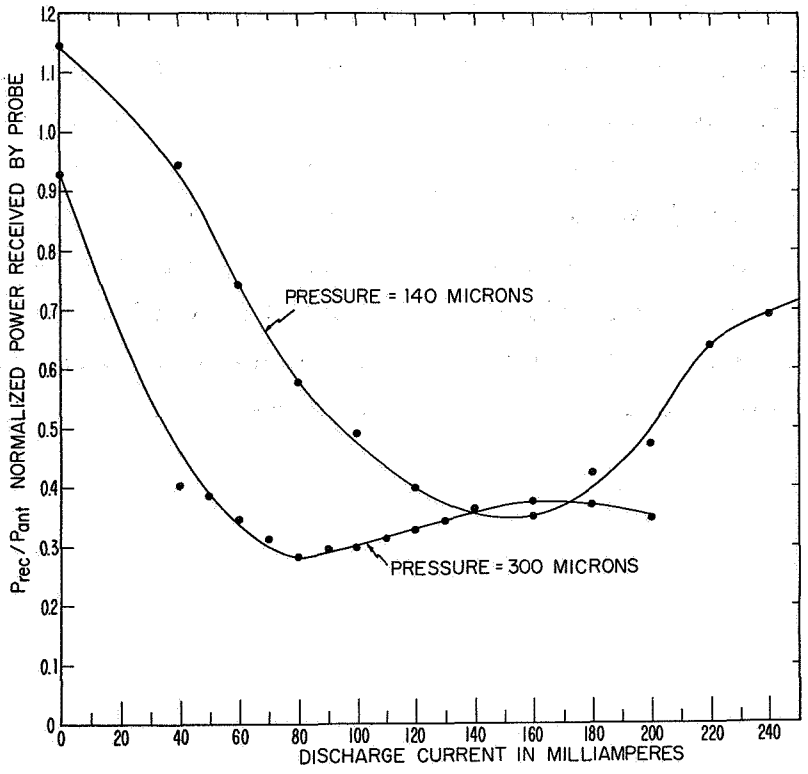

FIG. 24 NORMALIZED POWER BY THE PROBE AS A FUNCTION OF THE DISCHARGE CURRENT.

of the electric field near the antenna. At antiresonance the rf antenna current should decrease sharply, causing a similar decrease in the rf near field measured by the probe. These results are shown in Fig. 24. The signal picked up by the probe $P_{rec.}$ was normalized with respect to the power fed to the main transmitting antenna $P_{ant.}$ under investigation. The input power to the antenna was determined by using two directional couplers in conjunction with balometers to measure both the incident and the reflected power from the antenna. As the antenna length is increased in small increments, the susceptance of the antenna increases correspondingly. In order to keep the antiresonant frequency unchanged, the inductive element of the plasma must decrease. This makes the resonance curve shift to a lower discharge current or lower plasma frequency. But still the plasma frequency should be slightly higher than the operating frequency. The conductance of the antenna also increases with length, and the Q of the resonant circuit becomes smaller. These effects are illustrated in Fig. 25.

ACKNOWLEDGMENT

The authors thank Professor R. W. P. King for his helpful discussions and advice during the course of this investigation. They also extend their appreciation to Messrs. R. Wanser and A. Cajolet for their skill and patience in the fabrication of the glass tubes and vacuum apparatus, and to Messrs. D. MacMillan, F. M. Welch, and C. H. Sampson for their assistance in the design and construction of the experimental equipment. The Semi-con matrix-type cathodes were provided by the Electronics Components Laboratory, U. S. Army Electronics Command at Fort Monmouth, New Jersey.

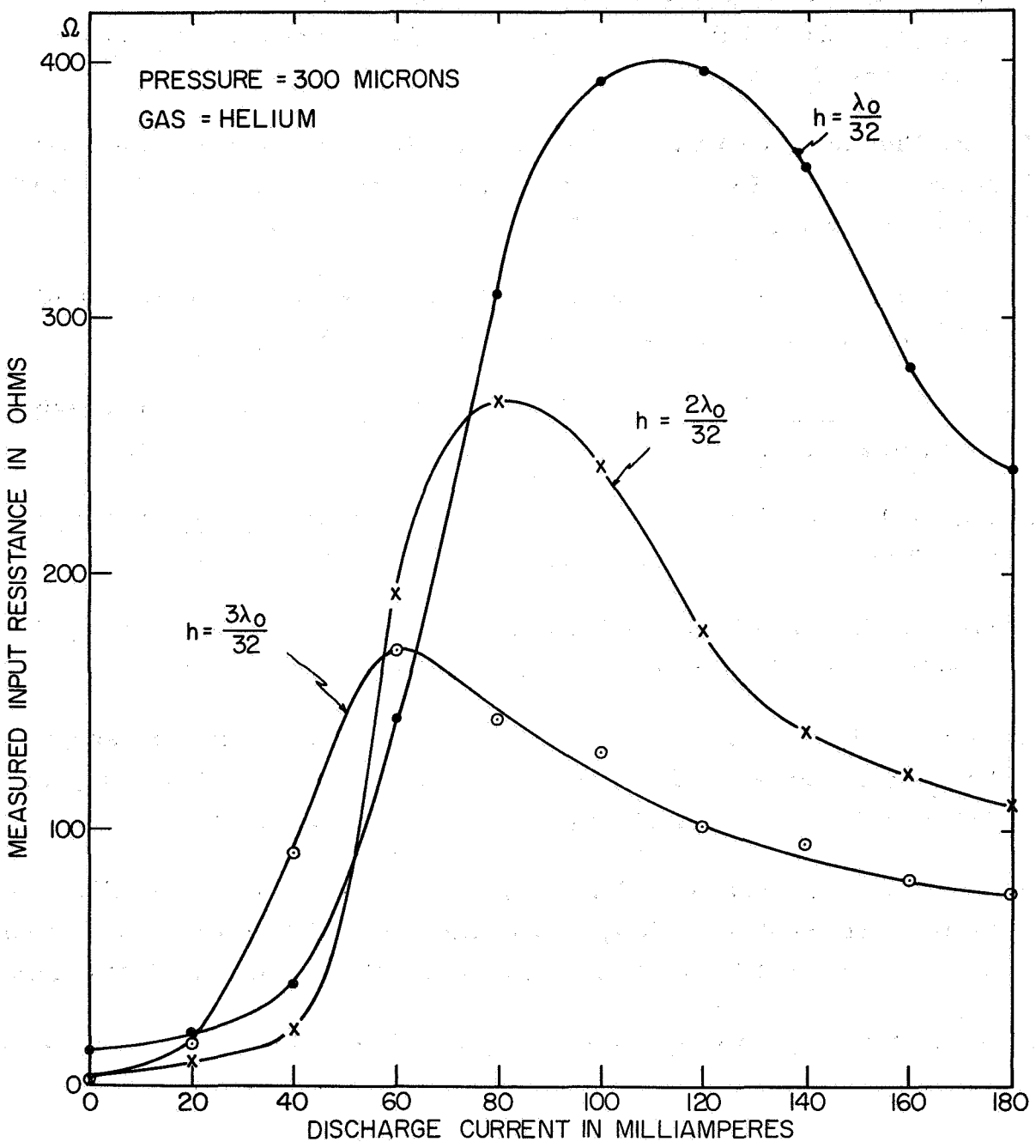

FIG. 25 MEASURED INPUT RESISTANCE AS FUNCTION OF DISCHARGE CURRENT FOR VARYING LENGTHS OF ANTENNA

REFERENCES

1. Seshadri, S.R., "Radiation from an Electric Dipole in a Plasma Column," Proc. IEE (London), Vol. 112, No. 2 (February 1965), pp. 249-253.

2. Ting, Chung-Yu, "A Theoretical Study of Dielectric-Coated Cylindrical Antenna," Cruft Lab. Tech. Report No. 506, Harvard University, Cambridge, Mass. (1966).

3. Tamir, Theodor, and Palócz, Suzanne, "Surface Waves on Plasma-Clad Metals Rods," IEEE Trans. on Microwave and Techniques, Vol. MTT-12, No. 2 (March 1964), pp. 189-196.

4. Ting, Chung-Yu, "Infinite Cylindrical Dielectric-Coated Antenna," Radio Science, Vol. 2, No. 3 (March 1967), pp. 325-335.

5. Loeb, L.B., Basic Processes of Gaseous Electronics, 2nd ed. (Beverly, California, University of California Press, 1960), pp. 329-373.

6. Heald, M.A., and Wharton, C.B., Plasma Diagnostic with Microwaves (New York: John Wiley and Sons., Inc., ed. 1965), pp. 155-163.

7. Parker, J.V., "Collisionless Plasma Sheath in Cylindrical Geometry," Physics of Fluids, Vol. 6 (1963), pp. 1657-1660.

8. Rama Rao, B., and Scott, L.D., "Plasma Profile Investigation Using a Multimode Cavity Perturbation Technique," Cruft Lab. Tech. Report, Harvard University, Cambridge, Mass. (to be published).

9. Levitskii, S.M., and Shashurin, I.P., "Test of Probe Method Applicability to the Measurement of Charge Concentration in High Frequency Discharge," Radiotekhnika i Electronika (English translation), Vol. 4(2)(1959), pp.8-16.

10. King, R.W.P., Transmission Line Theory (New York: Dover Publications, Inc., 1965), p. 278.